To be submitted to JGR-Oceans

Studies of Antarctic Sea Ice Concentrations from Satellite Data and their Applications

Josefino C. Comiso

NASA/Goddard Space Flight Center, Code 971, Greenbelt, MD 20771

Konrad Steffen

CIRES, University of Colorado, Boulder, Colorado CO 80309-0216

ABSTRACT

Large changes in the sea ice cover have been observed recently. Because of the relevance of such changes to climate change studies it is important that key ice concentration data sets used for evaluating such changes are interpreted properly. High and medium resolution visible and infrared satellite data are used in conjunction with passive microwave data to study the true characteristics of the Antarctic sea ice cover, assess errors in currently available ice concentration products, and evaluate the applications and limitations of the latter in polar process studies. Cloud-free high resolution data provide valuable information about the natural distribution, stage of formation, and composition of the ice cover that enables interpretation of the large spatial and temporal variability of the microwave emissivity of Antarctic sea ice. Comparative analyses of co-registered visible, infrared and microwave data were used to evaluate ice concentrations derived from standard ice algorithms (i.e., Bootstrap and Team) and investigate the 10 to 35 % difference in derived values from large areas within the ice pack, especially in the Weddell Sea, Amundsen Sea, and Ross Sea regions. Landsat and OLS data

show a predominance of thick consolidated ice in these areas and show good agreement with the Bootstrap Algorithm. While direct measurements were not possible, the lower values from the Team Algorithm results are likely due to layering within the ice and snow and/or surface flooding, which are known to affect the polarization ratio. In predominantly new ice regions, the derived ice concentration from passive microwave data is usually lower than the true percentage because the emissivity of new ice changes with age and thickness and is lower than that of thick ice. However, the product provides a more realistic characterization of the sea ice cover, and are more useful in polar process studies since it allows for the identification of areas of significant divergence and polynya activities. Also, heat and salinity fluxes are proportionately increased in these areas compared to those from the thicker ice areas. A slight positive trend in ice extent and area from 1978 through 2000 is observed consistent with slight continental cooling during the period. However, the confidence in this result is only moderate because the overlap period for key instruments is just one month and the sensitivity to changes in sensor characteristics, calibration and threshold for the ice edge is quite high.

1. Introduction

Accurate quantification of sea ice concentration from satellite passive microwave data is important because the latter provide the only long term and consistent day/night and almost all weather coverage of the sea ice cover in the Polar Regions. Sea ice concentration data are used to derive large-scale daily and monthly ice extents that are utilized in variability studies and trend analysis of the ice cover. They are also used to quantify the area covered by open water and thin ice in polynyas and divergence regions, which are in turn utilized to estimate vertical heat and salinity fluxes in these regions. Accuracy is important since it is necessary to detect the few

percent fraction of open water within the footprint of the satellite sensor that can make a big difference in the calculation of these fluxes (*Maykut,* 1978). Accuracy is also needed to validate currently observed changes in the ice cover (*Jacobs and Comiso*, 1993; *Bjorgo et al.*, 1997; *Cavalieri et al.*, 1997; *Rothrock et al.*, 1999)

Sea ice concentrations have been derived from the single channel Electrically Scanning Microwave Radiometer (ESMR) using a simple mixing algorithm that uses climatological surface temperatures to correct for temperature effects (*Comiso and Zwally,* 1982; *Zwally et al.*, 1983; *Parkinson et al.*, 1987). With the launch of the Scanning Multichannel Microwave Radiometer (SMMR), new algorithms that make use of the frequency and polarization dependence of the emissivity of the ice surface were developed, among which are the NASA Team Algorithm and the Bootstrap Algorithm (*Cavalieri et al.*, 1984; *Comiso et al.*, 1984; *Comiso*, 1986). These two algorithms were later adapted for the processing of Special Scanning Microwave Imager (SSM/I) data when the latter was launched in 1987 and have been used to generate continuous time series of ice data from 1979 to the present. These two algorithms also provide the basis for the development of new algorithms for the new Advanced Microwave Scanning Radiometer (AMSR) to be launched aboard the EOS-Aqua and NASDA-Adeos2 satellites. *Steffen et al.* (1992) summarizes the estimation of geophysical parameters using passive microwave algorithms. A comparison of the monthly ice concentrations derived from these two algorithms for the whole year of 1992 has been made and the results show good consistency in the Central Arctic in winter but large discrepancies in the Antarctic and seasonal regions of the Arctic in winter and the perennial regions in the summer (*Comiso et al.*, 1997). The differences in ice concentration are as large as 35 % in large areas of the Weddell, Ross, and

Amundsen Seas. A similar discrepancy has been identified earlier using Landsat MSS imagery to compare with the NASA Team ice concentration in the Weddell Sea on September 18, 1988 but was not used in the comparative analysis (*Steffen and Schweiger*, 1991). For studies of heat and salinity fluxes, mass balance, and modeling in the polar regions, it is important, as indicated earlier, that such discrepancies are resolved.

The key objectives of this study are to make use of passive microwave data in conjunction with available cloud free high and medium resolution data (a) to fully characterize the spatial and seasonal characteristics of the Antarctic sea ice cover; (b) gain insights into the large differences between the Bootstrap and the NASA Team algorithms as described by *Comiso et al.* (1997); and (c) to assess the value as well as limitations of ice concentration products currently used in polar process studies. In this study, we make use of data from Landsat, Advance Very High Resolution Radiometer (AVHRR), and Defense Meteorological Satellite/Operational Linescan System (DMSP/OLS). Landsat data, which have resolutions of either 30 m for Thematic Mapper (TM) and 82 m for Multispectral Scanner (MSS), clearly provide the resolution needed to get an accurate estimate of open water fraction during cloud free daytime conditions. It should be noted, however, that even at these resolutions, there are sometimes ambiguities in the interpretation of the data. For example, the dimensions of ice cover features, such as leads and pancakes, can be smaller than the 30-m resolution. Nevertheless, linear features such as leads with high contrast (dark lead in white ice) can be resolved to within 1/3 of the pixel size of the sensor (*Steffen and Schweiger*, 1991) and even in the worse case scenarios, the high-resolution data are likely the best validation tool available and provide at least the upper limit in the percentage of open water. The OLS and AVHRR data, have even

coarser resolutions at 600 m and 1.2 km, respectively, but they provide substantially larger spatial coverage and they enable extrapolation of results from limited number of Landsat data to a large fraction of the Antarctic sea ice cover.

2. Characteristics of the Antarctic Sea Ice Cover

The sea ice cover is a continuously evolving material from the time of formation to the time it melts. It starts with the accumulation of frazil ice at the surface into a loosely assembled ice sheet, called grease ice (Fig. 1a), and then a solid sheet in the form of nilas or pancake (Fig. 1c) depending on environmental conditions (*Allison*, 1981; *Steffen*, 1986; *Ackley et al.*, 1990). The ice sheet then grows in size and thickness through thermodynamics and through rafting (Fig. 1c,d) and ridging (Fig. 1e), the latter due to wind, waves (Fig. 1b), and tidal effects. Sea ice with thickness of about 30 cm is called young ice (Fig. 1f), which becomes first year ice as it gets thicker and acquires a snow cover. More detailed characterization of the physical properties of the sea ice cover is described elsewhere (e.g., *Weeks and Ackley*, 1986; *Eicken et al.,* 1991; *Tucker et al.,* 1992). The presence of relatively thick ice cover serves to suppress the effect of waves on ice breakup causing the formation of an almost continuous ice sheet a few hundred meters beyond the ice edge. The ice sheets are vast in extent but are seldom horizontally homogeneous and are occasionally broken by tides, waves, and strong wind to form leads. A typical Antarctic ice sheet in winter taken during the 1989 Weddell Gyre Experiment with R.V. Polarstern is shown in Figure 2. The photograph shows indications of ridging and flooding in the ice sheet and the presence of a lead about 150 m wide. When an ice floe survives at least one summer, it becomes a multiyear ice floe. Differences in the history of formation and the effects of wind and weather cause the ice cover to become inhomogeneous and/or regionally different.

To gain insights into the seasonal and spatial variability in the small-scale characteristics of the ice cover, we make use of Landsat images taken from areas indicated in Figure 3. The large seasonality in the Antarctic sea ice extent is well known (*Zwally et al.*, 1983). Less known is the large scale seasonality in the physical properties of the Antarctic sea ice cover. Such seasonal changes in the physical characteristics are vividly illustrated by two Landsat TM satellite images in the vicinity of Cape Batterbee (64.31° S, 54.50 ° E) (Fig. 3, boxes 1 and 2). The first scene (Fig. 4a) represents the summer/early-fall conditions during freeze-up, with new ice forming along the coastal region, extending up to 70 km off-shore. The ice cover consists primarily of young ice, a mixture of slush, shuga and possibly pancakes ice. Shuga is an accumulation of spongy white ice lumps, a few centimeters across. It is formed from grease ice or slush (*Steffen,* 1986). With the interaction of surface wind and waves, shuga lines up along the wind direction and forms the characteristic ice bands which can been seen in the first Landsat image (Fig. 4a) as well as in the aerial photograph (Fig. 1a). Surface waves can be identified in the Landsat sub-scene (Fig. 4b, 12 km x 12 km). Icebergs are also visible in this image, leaving an open water path in the shuga ice cover while traveling with the ocean current. The NCEP reanalysis pressure field of the 500 mb geopotential height shows a low pressure cell east and west of Cape Batterbee with a weak high pressure ridge running south-north along the 60° E Longitude (Fig. 4c). Given the low pressure gradient over the region, we would not expect strong surface winds in the Cape Batterbee region. According to the NCEP reanalysis (Fig. 4d), the 2-m air temperature was just a few degrees below freezing over the ocean region at Cape Batterbee, indicating that the ice cover starts to form. There is no fast ice along the coast.

Sea ice conditions are quite different in spring for the same region off Cape Batterbee

(Fig. 3, box 2), shown in the Landsat TM image, just eight months later (Fig.5). The pack ice is pushed away from the coast by the katabatic airflow, leaving a thin ice region of 10-20 km (Fig. 5a, c). To the east of Cape Batterbee, fast ice in the Magnet Bay is still attached to the coast, preventing numerous tabular icebergs from drifting with the pack ice (Fig. 5b). The pack ice is heavily broken, with floe sizes ranging from tenths of kilometers to sub-pixel resolution (Fig. 5d). It is interesting to note that the individual ice floes are composed of a matrix of floes frozen together. By using the spectral channels 3 (620-690 nm), 4 (760-900 nm) and 5 (1550-1750 nm) in a color composite image (red-green-blue: channels 3,4,5), the different floes can be readily identified by their lighter color (Fig. 5d). Also remnants of melt lakes can be identified on several of the floes by their dark appearance. Most of the dark ocean surface is actually covered with nilas, and ice type of only 5-10 cm in thickness. This can only be seen by stretching the dynamic range (8 bit) of the TM scene (Fig. 5c). According to the NCEP reanalysis air temperature field, sub-freezing temperatures (~266 K) were predicted for the ocean region on that date.

The circumpolar nature and general characteristics of the Antarctic sea ice cover are illustrated in the AVHRR images in the visible channel during the last weeks of April and November 1989 (Figs. 6a and 6b). The data are weekly averages derived from AVHRR Global Area Coverage (GAC) data and mapped into a 6.25 by 6.25 km grid as described by *Comiso* (2000). Although the resolution is relatively coarse, these images are still at a much better resolution than the passive microwave images (Figs. 6c and 6d) and provide a means to assess independently the general nature of the ice cover during the growing and melting seasons. Polynyas, especially near the coastal regions, are shown in the AVHRR images as relatively

darker than the thicker ice cover even when they are already covered by new ice. At the marginal ice zones, the ice cover is also shown to be grayish and sometimes difficult to discriminate from open water. But overall, the images provide an idea about the regions of high consolidation and areas of divergence or active ice formation.

The color-coded images in Figures 6c and 6d correspond to sea ice concentrations derived using the Bootstrap Algorithm for the periods corresponding to those of 6a and 6b, respectively. Overall, there is a good coherence in the images with the gray areas in the AVHRR satellite image corresponding to the relatively low concentration ice areas depicted in the passive microwave data. While the signatures look similar for both visible and passive microwave, the same values of ice concentrations from the two periods represent a very different type of ice cover as discussed previously. During the growth period in autumn, large areas in the ice covered region look gray in the AVHRR map but the true ice concentration is actually higher than that provided by the passive microwave data, the main reason being that new (or thin) ice types have lower reflectivities and microwave emissivities than the thicker ice types. On the other hand, during the melt/decay period, the gray (low reflectivity) areas correspond proportionately to the relatively low concentration ice cover depicted by the corresponding passive microwave data. A more detailed analysis and discussion of this phenomenon will be provided in the following sections.

3.0 **Determination of Ice Concentration from Satellite Data**

Sea ice concentration has been defined as the fraction of ice covered areas within the field of view of satellite observation. Although the resolution of passive microwave satellite data is relatively coarse at about 25 km by 25 km, the use of a mixing algorithm makes the derived ice

concentration basically resolution independent. The algorithms, however, assumes that within the ice pack, we either have thick (white) ice or open water. While dominantly the case in spring and summer, the definition is not as easy to apply in winter because during this time of ice growth, sea ice is a continuously evolving ice sheet or cakes that changes in thickness and character while at the same time, its passive microwave emissivity, and hence brightness temperature changes as well. In general, the derived ice concentration provides a realistic physical representation of the ice pack since it enables identification of locations of important features, such as leads and polynyas, even if the surface of the latter is newly frozen. This in turn provide the means to better quantify heat and salinity fluxes as well as the approximate volume of the ice cover. The Landsat (and other visible channel) ice concentration retrieval makes use of the reflection of solar light and therefore can distinguish not only open water and white ice, but also young ice, gray and gray-white ice types. We will use the latter to better understand ice retrievals from passive microwave sensors and how such retrievals could be better utilized for polar process studies.

3.1 NASA Team and Bootstrap Algorithms

The brightness temperature observed by the satellite sensor originates dominantly from the Earth's surface but in part from the atmosphere and from outer space. At the frequencies used in ice algorithms, the spatial variations in the effects from the atmosphere and that of outer space are assumed to be small (*Comiso and Zwally*, 1982). The basic equation used by the two algorithms for deriving sea ice concentration, C_I, is as follows:

$$T_B = T_I C_I + T_O (1 - C_I) \qquad (1)$$

where T_B is the satellite observed brightness temperature, T_I is the brightness temperature of ice, and T_O is the brightness temperature of open water within the Antarctic ice pack. This equation is applicable to any frequency or polarization channel. The unknowns in this equation are T_I and T_O. T_I is a function of the ice emissivity and the emitting ice temperature, both of which changes spatially and temporally. Within the ice pack, T_O is assumed constant in winter since open water in the region have uniform emissivity and temperature but is adjusted slightly during the summer because of warmer temperatures and slightly different emissivity due to larger areas of open water that is more vulnerable to foam and surface roughness due to wind and other external factors. If To and T_I can be determined very accurately, equation 1 should provide a good estimate of open water within the pack regardless of sensor resolution. The two algorithms make use of different sets of channels and different techniques to obtain T_I as described elsewhere (*Cavalieri et al.*, 1984; *Comiso et al.*, 1984; *Steffen et al.*, 1992; *Comiso et al.*, 1997). If the assumptions are satisfied in both techniques, the results from the two algorithms should be in good agreement. Although there are many areas where there is general agreement, there are also large areas where they disagree, as pointed out in *Comiso et al.* (1997). More details about the differences in the techniques that lead to differences in the results will be discussed in a later section on comparative analysis. The error in the retrieval of ice concentration from passive microwave data has been estimated at about 5 to 10% during autumn and winter and about 10 to 20% during the spring and summer.

3.2 Landsat Processing

For detailed studies of ice distributions and characteristics and validation of the DMSP SSM/I ice algorithms, 7 cloud-free Landsat scenes around Antarctica were selected (Fig. 3),

providing a variety of ice concentrations and ice types (Table1). The digital Landsat data were transformed to a polar stereographic grid with 25 km analysis cells to match the SSM/I derived ice concentrations from the NASA Team and Bootstrap algorithms. Ice concentrations have been derived from Landsat MSS and TM images in a number of previous studies using different methods, which are based on the reflectivity difference between water and ice (*Hall*, 1980; *Ito,* 1985; *Comiso and Zwally*, 1982). In this study, we used the methods described by *Steffen and Schweiger* (1991) depending on the ice types present in the Landsat image; (1) a maximum likelihood classifier utilizing reflectivity differences between ice types when different surface types such as open water/nilas, gray ice, gray-white ice and white ice are present during spring and fall, and (2) a tie point algorithm that accounts for sub-resolution ice features when only open water and white ice are present in summer. The Landsat data thus enable the determination of true open water and the fraction of different new ice types within the footprint of the passive microwave sensor.

The Landsat MSS instantaneous field of view (IFOV) that can be defined as the ground area viewed by the sensor at a given instant in time is nominal at 82 m x 82 m for Landsat 4 and 5. The MSS scene consists of 2400 scan lines, each composed of 3240 pixels representing an area of 170 km x 185 km. The Landsat TM data were calibrated using the Environment for Visualization Images (ENVI) software. The physical antenna temperatures for channel 6 (the thermal infrared channel) were derived by using the EOSAT-supplied conversion coefficients. The visible, near-, and mid-infrared channels 1 to 5 have an IFOV of 30 m, whereas the thermal infrared channel 6 has only an IFOV of 120 m. The TM imagery is analogous to MSS imagery with respect to aerial coverage.

Owing to the high reflectance levels of snow and ice in the blue-green spectral range, TM channel 1 (450-520 nm) is frequently saturated and can be utilized for ice classification only under low sun angle illumination conditions. Reflectance differences between thin ice types and ice-free ocean are greatest in the red and near infrared range, so that TM channels 3 (630-690 nm) and 4 (760-900 nm) are most suitable for the determination of ice concentration. Further, channel 6 (10.4-12.5 μm) is very useful for thermal mapping and to distinguish between ice-free, different young ice types, and first-year ice/old ice. The thermal channel was not used as a primary channel for TM ice typing. For Landsat MSS, the channels 2 (600-700 nm), 3 (700-800 nm) and 4 (800-1100 nm) were used for ice typing. For the tie point algorithm (summer conditions), only TM channel 4 or MSS channel 4 was used.

Ice type classification from Landsat imagery is possible because ice reflectivity is related to ice thickness. The thinner the ice, the darker it appears in the imagery. Consequently, the digital numbers or the spectral radiance per wavelength values ($W\ m^{-2}\ sr^{-1}\ \mu m^{-1}$) of the imagery can be related to ice thickness. Comparison of Landsat MSS derived ice thickness with ground reflectance measurements during the Arctic Ice Dynamic Joint Experiment indicate that it is possible to infer ice thickness up to 0.6 m with an accuracy of ± 0.05 m when climatologically derived growth rates are incorporated in the calibration [*Hall*, 1980].

Selection of points belonging to each surface type such as ice-free, nilas, gray ice, gray-white ice, thin first-year ice, medium and thick first-year ice was done using the ENVI software. For each of the seven ice categories, pixels were visually identified and selected from TM channel 4 or MSS channel 4 image enhanced to show the greatest separation between each category and all the others, typically over 1000 points from several image sub-regions. After a

sufficient number of training data points for each category was accumulated, ENVI was used to generate ice type class statistics (means, standard deviations) for these points using TM channel 4 or MSS channel 4. Having obtained the statistics for each category, we used them in a maximum likelihood classifier, in which previously unclassified data points are assigned to the class to which they are most likely to belong. Following classification, ice concentrations are calculated using data inside the corresponding SSM/I 25 km x 25 km grid boxes.

The procedure for sea ice concentration calculation during summer from Landsat imagery was developed by *Comiso and Zwally* [1982], and is based on the idea that during periods when no new ice formation occurs, the spectrum of classes is reduced to open water and white ice. If open water and white ice are the only two classes present, the assumption can be made that all brightness values in between those classes must represent ice concentrations at sub-resolution. Locations where a known state is assumed (i.e. 100% ice, 100% open water) are known as tie points. This algorithm thus accounts more realistically for the presence of ice floes smaller than the Landsat MSS or TM resolution, but will introduce errors when ice reflectance is variable. The ice concentration (C_I) is derived using the equation

$$C_I = [(B_x - B_{OW})/(B_{WI} - B_{OW})] * 100 \qquad (2)$$

where,

B_x = Brightness value of the Landsat pixel,

B_{OW} = Brightness value for open water, and

B_{WI} = Brightness value for white ice minus one standard deviation.

Tie points were found using training areas for open water and large white ice floes, where B_{WI}

represents the mean brightness for that floe minus one standard deviation. In the subsequent analysis the tie-point algorithm was used to calculate ice concentrations for images during summer and early fall conditions, when open water/black nilas and white ice were the only surface classes present and meltponding was not apparent in the imagery.

Unresolved ice features such as leads and ice floes smaller than the Landsat field-of-view will be misinterpreted causing an error in the derived ice concentration. These errors have to be considered in light of the fact that in some cases, for example during break up, the relative proportion of ice features that are smaller than IFOV of the MSS sensor could be relatively large. The accuracy of Landsat ice concentration retrieval is discussed in *Steffen and Schweiger* (1991).

3.3 *OLS Processing*

Because of much coarser resolution than Landsat, OLS data are not as suitable as the former for discriminating new, young, and thick ice types and different surfaces. However, OLS data have good enough resolution to provide at least the lower limit of the ice concentration. Ice concentration is derived from OLS data by using the thresholding method in the winter or cold months and a mixing algorithm that makes use of equation 2 in the summer, when the air temperature is above freezing. The thresholding method was done through the use of an open water threshold on an image by image basis. In each image, open water signature is identified by inspection through computer graphics interaction and using contrast stretching and other image enhancement techniques, if necessary. The threshold for open water is determined through analysis of the frequency histograms of pixels in predominantly open water areas. A value that is 2 standard deviations higher than the peak of water signature is usually chosen as the threshold. In highly compact regions in which the width of leads is comparable to the size of each pixel, the

threshold that is used is that corresponding to the pixel with the highest radiance that represents open water in the image.

The mixing algorithm is used (instead of the thresholding technique) during spring and summer when the ice cover is undergoing breakup and the formation of new ice is minimal. The algorithm makes use of equation 2 and tie points for white ice and open water that are determined through statistical analysis of the radiances of white ice and open water in the image. However, during melt conditions, the white ice usually turn to gray and the tie point for thick ice has to be re-adjusted to minimize errors. While the techniques used for Landsat and OLS are basically the same, the ice concentrations derived from OLS data are biased and generally lower than those determined from Landsat data because in the former, the derived open water may be contaminated by new ice or a small fraction of thick ice that are not detected due to limited resolution. The error in the estimate of ice concentration from OLS data has been estimated to be about 10 to 20% in general but is expected to be much smaller in consolidated ice regions during winter and dry surface conditions.

4.0 Comparative Analyses of Derived Ice Concentrations

Comparative analyses in this study are confined to data from the two algorithms that are most used in climatological and polar process studies and are archived in data centers. The choice of study regions is influenced by the results of the *Comiso et al.* (1997) study and the availability of cloud free visible channel data in the area of interest. Color-coded maps of the monthly averages (July, August, September, and October 1992) for Team and Bootstrap algorithm results and the differences are shown in Figure 7. The images show that the areas of largest discrepancies are in the middle of the pack and especially in the Weddell Sea and the

Amundsen/Ross Seas region. The main emphasis of this study is thus to evaluate the true ice conditions in these two areas.

The regions of large discrepancies between the Team and Bootstrap Algorithms, as discussed previously, are also regions of relatively low brightness temperatures. To gain insights into the surface emission characteristics that may cause the discrepancies, daily brightness temperature maps of the Antarctic region on September 30, 1992 at 6 SSM/I frequencies and polarizations are presented in Figure 8. It is apparent that the contrast in brightness temperature between the open ocean and sea ice is frequency dependent and is largest at 19 GHz. Such contrast is necessary for accurate retrieval of ice concentration and hence the use of one or both of these channels in the algorithms despite poorer resolution. In Figure 8, the sea ice-covered region is easily identified in the 19 GHz maps while it is not so well defined in the 85 GHz maps. Within the ice pack, spatial changes are also apparent with much higher sensitivity at the higher frequencies to spatial changes in surface emissivities that are related to surface or subsurface scattering properties. It should be noted that at 37 GHz and higher frequency channels, the emissivity of open water can be higher than that of sea ice.

To show more quantitatively the frequency dependence over water and sea ice at various frequencies, plots of brightness temperatures over a transect along 33° W (see short line in Fig. 8) are shown in Figure 9. The approximate location of the ice edge is represented by the vertical dotted line. To the left of this line is open water while to the right is the sea ice cover. At the marginal ice zone, all the SSM/I channels except the 85 GHz channels show marked increase in brightness temperature from open water areas to the consolidated ice areas. The 19 GHz channels show the largest jumps in brightness temperature, followed by the 22 GHz channel and

then the 37 GHz channel. At the ice edge (dotted line), there is almost no change in the 85 GHz brightness temperatures at both channels but within the pack, the vertical channel values slowly declines while the horizontal channel values are almost constant. Also, data from all the channels appear to be coherent and sensitive to the same surface effects, except those from the 85 GHz channels, which appear to be sensitive to other factors. The plots show that despite poorer resolution at 19 and 37 GHz channels, the ice edge provided by these channels are more well defined, consistent, and dependable than those provided by the 85 GHz channels. The vertical dotted line in the plots corresponds to 10-20% ice concentration, which is used for ice edge and ice extent determinations. For trend analysis of the ice extent, ability to accurately infer the ice concentration value of the ice edge consistently is very important as will be noted later.

Scatter plots between brightness temperatures of two SSM/I channels and between gradient and polarization ratios, as defined in *Comiso et al.* (1997), are presented in Figures 10a and 10b. In the Bootstrap Algorithm, the tie-point for 100% ice is along the line AD, as labeled in Figure 10a. In the NASA Team Algorithm, the tie-point for 100 % ice is along the line AB in Figure 10b. Ice concentration is derived using a multichannel version of equation (1) and it is apparent from the scatter plots that there are a lot more data points along the line AD (used by the Bootstrap Algorithm) than along the line AB (used by the Team Algorithm). The question is thus whether or not the data points along the line AD really represent 100% ice cover. It is through the use of validation data sets, such as the OLS, AVHRR, and Landsat data that we try to establish which assumption is correct. The OLS data have wide swath (about 1600 km) and cover a large fraction of the Antarctic ice covered regions while the Landsat images are only

about 170 km by 185 km in area and provide more limited coverage. The geolocations of the Landsat images used in this study are shown in Figure 3. Since a large fraction of these available images are near the coastal areas (they were originally requested for continental boundary studies), the use of other images with intermediate resolution (i.e., OLS and AVHRR) is important even just to establish the upper limit in the ice concentration in other areas and other time periods.

4.1 The Weddell Sea

4.1.1 Large scale comparison with OLS images

The difference in ice concentrations in the Antarctic, as derived from the Bootstrap and Team algorithms, is largest in September as reported in *Comiso et al.* (1997) and shown previously. It is fortuitous that a generally cloud free OLS image of the Weddell Sea was acquired on September 30, 1992. The difference in the retrieval from both Bootstrap and Team algorithms are even larger for these daily maps than those from the monthly averages with the Bootstrap values generally larger than the Team values, the largest difference being about 40% in the central Weddell Sea.

Selecting three study regions in the OLS image on September 30 that are not contaminated by clouds (i.e., boxes 1, 2, and 3), the retrieved ice concentration data from OLS and the Team and Bootstrap algorithms are shown in Figure 11. The ice concentrations derived from OLS, Bootstrap, and Team Algorithms are 96.1%, 96.3%, and 74.2%, respectively in box 1, and 98.7%, 98.8%, and 74.8% in box 2. The average difference between the OLS and Bootstrap ice concentrations is 0.8% while that between the OLS and the Team ice

concentrations is 22.9%. In box 3, the corresponding values are 98.2%, 98.8%, and 94.3%, indicating good agreement in some regions. Slightly to the north, the discrepancies between the Bootstrap and Team values are apparently even larger but were not quantitatively studied because of cloud effects on the OLS image. In Figure 10a and 10b, the data points corresponding to box 1, box 2, and box 3 are shown in blue, green and red, respectively, to better understand how data from each of these boxes are represented relative to the tie points used by the two algorithm techniques. It is apparent that in these areas of consolidated ice cover, the polarization ratio is very variable and deviates a lot from the tie point AB in Figure 10b, suggesting polarization effects due to layering in the snow or snow-ice interface, as well as other factors, as described by *Mätzler et al.* (1984). In Figure 10c, plots of the frequency distribution of ice concentrations derived from both algorithms are shown and it is apparent that the distribution for consolidated ice data (near 100% C_I) are very different with the standard deviations being ±3.4%, and ±8.1%, respectively, for the Bootstrap and NASA Team data. The much larger standard deviation in the Team data than the Bootstrap data reflects the much larger scatter of consolidated ice data in the scatter plot of Figure 10b than that of Figure 10a and hence larger uncertainties in the former. A similar analysis was done with a relatively cloud free image on October 7, 1992 (Fig. 12) to illustrate that the effect is persistent and likely associated with surface or subsurface characteristics. In this case, the ice concentrations from OLS, Bootstrap, and Team are 98.0%, 97.0%, and 80.3%, respectively, in box 1 and 98.4%, 96.4%, and 98.1% in box 2. Again, the Bootstrap results are in general agreement to those of OLS and the discrepancies with the Team results further north are bigger than those in the southern region. The areas of large discrepancies are just beyond the transition from the marginal ice zone to the consolidated ice pack.

4.1.2 Small-scale comparison with Landsat images

It is again fortuitous that a cloud free Landsat image during September 18, 1988 in the same general area of large discrepancies is available as shown in Figure 13. Because of much higher resolution, the Landsat data have the accuracy requirement needed to evaluate the ice concentration product with high confidence and can be used to confirm the validity of the results from the OLS data. A Landsat image classified by ice types is shown in Figure 13c, with 89.6% white ice, 7.5% gray ice 2.5% nilas and 0.4% open water. Open water is only present in a north-south oriented leads as shown in a subset of the Landsat image (Fig. 13d). Even if the lower emissivities of gray ice and nilas were taken into account, the ice concentration expected from passive microwave data would be 98.3%. For this same region, the Bootstrap Algorithm yielded 100% ice concentration (Fig. 13b) while the Team Algorithm result was about 65% (Fig. 13b), as reported previously by *Steffen and Schweiger* (1991). Although only one high resolution image in the Weddell Sea area for this time period is available, it is apparent that the result from the Landsat analysis is consistent with those from the OLS analysis. It is also apparent that for this particular day, the location of large discrepancies between the Team and Bootstrap algorithms are in the same general area as that shown in the September 1992 data.

4.2 The Ross/Amundsen Seas

4.2.1 Large scale comparison with OLS images

The other area of large discrepancies between the Bootstrap and Team Algorithms is located in the Ross Sea/Amundsen Sea region. The results of comparative analysis of a relatively cloud free OLS image and SSM/I data, similar to that done in the Weddell Sea, are shown in

Figure 14. The ice concentrations derived from OLS, Bootstrap, and Team algorithms are 98.9, 95.0, and 79.1%, respectively, on September 1, 1995. Similar analysis (not shown) near the same area yielded corresponding values of 93.2, 91.5, and 77.4% on September 5, 1995 and 93.7, 93.6, and 82.5% on September 10, 1995. In these cases, the areas of large discrepancies are deeper into the pack and more isolated than in the Weddell Sea. It should be noted that the ice cover in the two regions as observed by the OLS data are usually highly packed and close to 100% in winter.

4.2.2 Small scale comparison with Landsat images

A Landsat TM scene of the Ross Sea summer ice conditions in a location indicated in Figure 3 has also been analyzed. The image acquired on December 16, 1988 showed a compact ice cover of approximately 125 km along most of the continental coast, and a well-defined ice margin (Fig. 15). Ice concentrations above 90% were derived using the two passive microwave algorithms and the Landsat threshold method for most of the pack ice region, whereas the mean ice concentration within the Landsat image (excluding ice shelves and land) was 73.0% for the Team Algorithm, 83.8% for the Bootstrap Algorithm and 89.2 % for the Landsat classification respectively. Both Bootstrap and Landsat ice concentrations provide similar spatial ice concentration variability with small discrepancies close to the land and along the ice margin. The NASA Team derived ice concentration shows a similar spatial pattern with up to 10% lower values in the pack ice region. Discrepancies along the continental coast are partly due to the different microwave signature of ice shelves imbedded in the pack ice.

The Landsat MSS image from the Amundsen Sea on December 29, 1990 showed some mid and low-level clouds, which however, did not hamper the ice typing (Fig. 16). Mid-level

clouds over sea ice were classified in the Landsat image due to their lower reflectivity compared to the ice surface. Low-level clouds did not affect the ice retrieval since they were semi-transparent and the open water regions covered by these clouds still had a distinct signature, which separated them from white ice. This classification would not have been possible during winter and spring periods where different ice classes are common. The Landsat retrieval revealed a mean ice concentration of 85%, whereas the passive microwave retrievals showed values of 83% for the Team Algorithm, and 90% for the Bootstrap Algorithm, respectively. Since this Landsat scene was well outside the coastal region (Fig. 3), land contamination of the passive microwave signal cannot be blamed for the ice concentration difference. However, the data used correspond to summer conditions when uncertainties in the retrieved microwave data are expected to be higher because of surface melt conditions.

4.3 Other Regions

Summer ice conditions were analyzed for the Bellinghausen Sea using a Landsat image in December taken at the location indicated in Figure 3. The ice cover comprised of large ice floes of up to 25 km in diameter with numerous small floes and some open water along the coast (Fig. 17). The land and shelf ice regions were excluded from the analysis. The Landsat ice classification using the threshold method revealed an ice concentration of 92%. The NASA Team algorithm underestimated the Landsat ice concentration by 8%, and the Bootstrap algorithm overestimated the Landsat derived ice concentration by 2%. Melt ponds were not apparent in the Landsat TM image, however, flooding of small ice floes was observed along the coastal polynya which probably explains the discrepancy of the NASA Team algorithm.

The ice cover along the southeast Antarctic coast (Fig. 3) was studied using a Landsat

TM scene from November 17, 1989. The scene comprised of a variety of different ice types, ranging from open water (27%), young ice and nilas (20%), gray and gray-white ice (8%) and white ice (45%) based on a tie-point maximum likelihood classification. Figure 18 shows the Landsat TM channels 5, 3, 1 in a combined red-green-blue composite image. In this channel combination, thin ice and flooded ice has a bluish color, and thin clouds have a reddish tone. Both passive microwave algorithms underestimated the ice concentration. The NASA Team algorithm showed only 51% ice concentration, a discrepancy of 22%, roughly the amount of young ice and nilas found in the Landsat classification. The Bootstrap retrieval with 70% ice concentration and a discrepancy of 3% seems to perform reasonable under these conditions.

4.4 Sensitivity to Temperature and Emissivity

As pointed out by *Comiso et al.* (1997), the retrieval of sea ice concentration is sensitive to spatial variations in surface ice temperature and emissivity. The larger sensitivity of the Bootstrap Algorithm than the Team Algorithm to ice temperature was also been pointed out but the spatial variability and the magnitude of the error has been estimated to be small in typical Antarctic conditions (*Comiso et al.*, 1992). This issue is further studied using surface temperatures derived from AVHRR data as described by *Comiso* (2000), an examples of which is a monthly average in September 1992 as shown in Figure 19a. As indicated in the image, there are significant spatial changes in temperature from the marginal ice zone and into the ice pack with the coldest being closest to the continent. Since the microwave emission detected by the satellite usually emanates from the ice surface, AVHRR surface data are converted to snow/ice interface temperature data using the regression results of *Comiso et al.* (1989). An ice concentration map derived using emissivity data (that makes use of the AVHRR data to correct

for temperature effects) is shown in Figure 19b while the difference map between the original and corrected results is shown in Figure 19c. As indicated, the differences in ice concentration between the two images are within about ± 2%. This indicates that the original technique does a good job in taking account of spatial variations in surface ice temperatures. This is consistent with the observed small spatial variability in the snow/ice interface temperature (standard deviation of about ± 2.5%) as reported by *Comiso et al.* (1989). The effect of temperature may be significant in ice areas where there is no snow cover, as in young ice areas, and where it is extremely cold, as the coastal regions of Antarctica. Future improvements in the algorithm will include the use of 6 GHz channel data to correct for temperature effects, as described by *Comiso and Zwally* (1997). Such algorithm would be most useful for data from the Advanced Microwave Scanning Radiometer, scheduled for launch on board EOS-Aqua and ADEOS-2.

It is apparent that the large disagreements between the Team and Bootstrap Algorithms are associated not with temperature but with the spatial variations in the emissivity (or polarization) of sea ice. Much of the spatial variations in emissivity is supposed to be taken into account through the use of a multi-channel algorithm (i.e., the use of AD or AB in Figs. 10a and 10b, respectively). As discussed previously, the use of polarization ratio is especially a problem in some ice surfaces because the horizontal polarization is more sensitive to some surface and subsurface characteristics (e.g., layering) than the vertical polarization as reported previously (*Mätzler et al.*, 1984; *Grenfell et al.*, 1994). The scatter plot in Figure 10b is an illustration that the polarization for consolidated ice, especially in primarily seasonal sea ice regions, can vary considerably. We have indicated earlier that some consolidated ice data points fall significantly to the right of the line AB, used as the tie point for 100% ice, causing the concentrations derived

from the Team algorithm to have values as low as 65%.

5. Applications

5.1 New Ice, Polynyas, and Flux Studies

Among the most important features of the sea ice cover are the polynyas and leads since these features can cause a profound influence on the ocean circulation and the Earth's climate system (*Gordon and Comiso*, 1988). The polynyas may be either coastal (latent heat) polynyas or deep ocean (sensible heat) polynyas. The coastal polynyas are usually caused by southerly wind that advects ice to the north exposing surface water to the extremely cold atmosphere and making this surface vulnerable to freezing. These coastal polynyas have been regarded as ice factories and are the site of formation of cold and dense bottom water that circulates around the globe. On the other hand, deep ocean polynyas as large as the state of California have been observed in Central Weddell Sea in the 1970s and are often the site of deep ocean convection that changes the vertical stratification of the water masses. The formation of ice in leads and advancing ice edges also cause horizontal changes in the salinity and density of the water masses. It is thus important that sea ice data could identify these features.

As indicated earlier, true open water areas within the pack that are formed by divergence due to wind forcing usually do not last very long. Within a few hours, the surface is filled by frazil ice that consolidates to form nilas or pancakes (Fig. 1c), the emissivity of which varies depending on thickness and is usually substantially different from that of thick ice (*Grenfell et al.*, 1992). This phenomenon is especially relevant along the coastal areas in the Antarctic, which have been regarded as ice factories because of high rates of ice formation. The coastal regions

are therefore noted for the abundance of new and young ice. The question of interest is how to characterize the presence of new and young ice in these regions. Since the surface is continuously evolving from grease ice to thicker ice types it is not easy to infer ice concentration because of time varying emissivity and even if successful, it is not certain that the results would be meaningful. Since open water freezes within hours in winter, the daily average data would provide practically 100% ice most of the time during this time period, considering that the error is about 5 to 10%. An algorithm that would identify a surface covered by grease ice as 100% ice concentration would therefore not show any feature within the ice pack. Areas of divergence and polynyas will have the same value as areas of thick ice cover. Since the fluxes from new and thin ice are an order of magnitude larger than those of thick ice (*Maykut,* 1978), the results from such an algorithm would be of very limited use.

Among the most active and persistent coastal polynyas in the Antarctic region are the Ross Sea and Terra Nova Bay polynyas. The location and size of these polynyas are depicted in the AVHRR image in Figure 20a with grayish signature. The corresponding ice concentration map shown in Figure 20b show values ranging from 60% near the Ross Shelf and Terra Nova polynya to 90% in the general vicinity. The true ice concentration is likely much higher but the derived product shows a more realistic characterization of the ice cover. Note that the true spatial distribution of ice in the region is difficult to infer from the AVHRR image because of cloud cover but suggestions of reduced ice concentration or new ice near the Ross Shelf and the Terra Nova polynya are apparent. Figure 21 are ice vector maps for the period (and other periods) derived from passive microwave data using the technique reported by *Kwok et al.* (1998), and indicate that the areas of 60% to 90% ice concentration are actually very active

areas. This implies that polynyas and leads are constantly being created causing the formation of new ice that gets advected to the north. The heat fluxes from these types of ice have been studied (*Steffen*, 1991) and the results show proportionate sensitivity of these fluxes to the derived ice concentrations. For example, because of lower emissivity than thick ice, retrieved ice concentration from nilas is about 70% while our estimate of heat flux from nilas is also about 70% of the difference of that from white ice (i.e., -45 watts m^{-2}), and open water (i.e., -785 watts m^{-2}) for a surface air temperatures of –20 °C.

Enhancements in the algorithms to increase the sensitivity to and hence the ice concentration for new ice cover is possible. The use of the Arctic Bootstrap algorithm that makes additional use of the 37 GHz (H) versus 37 GHz (V) in the algorithm (*Comiso*, 1986), provide higher ice concentrations in new ice areas, the reason being that sensitivity to new ice is higher at higher frequencies because of shorter penetration depths. The 37 GHz (H) is apparently less sensitive to thinner ice types than the 19 GHz (V) because of shorter wavelength and penetration depth. The use of the 85 GHz channels has also been explored for even greater sensitivity to the presence of new ice. Such technique has been utilized by *Markus and Cavalieri* (2000) to come up with a new Team algorithm that provides higher concentrations not just in new ice areas but also in other ice areas discussed in this paper. The 85 GHz data can provide useful information about the ice cover because of higher resolution but the contrast between ice and water at this frequency is not so good (see Fig. 9). Also, data at this frequency are highly sensitive to snow cover and to adverse weather conditions which are not uncommon in the Antarctic region.

A more complete information about the ice cover can be obtained by supplementing ice

concentration results with ice type classification results. The ability to delineate the location of different ice regimes, especially those of the new ice cover could come a long way to an improved characterization of the ice cover. The determination of ice class and ice concentration simultaneously would provide the tools for accurate estimates for heat and salinity fluxes and a full utilization of the microwave data for polar process studies. Some of the current ice classification techniques take advantage of multichannel differences in average emissivities in different ice regimes, as in *Massom et al.* (1999), but improvements in the technique and further validation are needed for accuracy in interpretation and better consistency.

5.2 Ice Edge, Extent and Trend Studies

The large contrast in the emissivity of ocean and ice at some microwave frequencies provides the means to easily find the location of the ice edge and hence the northern limit of the ice cover at a good temporal (less than a day) resolution. The emissivity of ice and open water are virtually indistinguishable near the ice edge until the ice concentration reaches about 10%. Figure 9 shows a gradual but consistent increase in brightness temperature at all SSM/I frequencies, except the 85 GHz channels, from open water region and into the ice pack. The ice edge can be consistently located by passive microwave data at a specific ice concentration level as long as the calibration and resolution of the sensors are consistent. The potential for errors associated with the use of data from different sensors with different resolutions and possibly different calibrations is illustrated in Figure 22. Yearly annual averages of extent from SMMR are compared with those from SSM/I in the plots using both Bootstrap and Team ice concentration data and it is apparent that trend results from the two algorithms are not consistent. The difference is partly due to the use of different techniques for estimating ice concentration

and hence the 15% ice edge (e.g., Fig. 9) and also in the masking of ice-free surfaces. It is also apparent that the differences between the Bootstrap and Team ice extent values changes from SMMR to SSM/I data. This may have something to do with differences in resolution which for SMMR and SSM/I are 30 km and 45 km, respectively, at 19 GHz. The Bootstrap and Team algorithms uses different combinations of both vertical and horizontal channels at 19 GHz and 37 GHz to derive ice concentration and therefore are not expected to provide identical ice extents since the position of the ice edges determined by the two techniques are different. It should be noted that a difference of about a pixel in the location of the ice edge causes a difference in the Antarctic ice extent of about 16% in the summer and 3% in the winter. This indicates that accuracy and consistency of summer ice data is important, especially when data from different sensors are assembled.

The satellite ice concentration data provide the most consistent record of ice extent and actual ice area within the ice pack. Long term records of monthly anomalies in ice extent, actual ice area, and average ice concentration derived with the Bootstrap algorithm are shown in Figure 23. The results of linear regression analysis, using the monthly anomalies, show a slightly positive trend for ice extent (Fig. 23a) and good consistency with that derived from yearly values in Figure 22. The trend for actual ice area (Fig. 23b) is, however, also shown to be higher than that of the ice extent. About 80% of the difference in the trends of actual ice area and ice extent can be explained by the apparent rate of increase in ice concentration (Fig. 23c) during the 20-year period. While efforts were made to make the data set consistent during the short overlap period between SMMR and SSM/I (about a month in winter) a bias may still exits since it is not known how the two compares during the other seasons, especially during summer, when a bias

of even just one pixel can cause a significant difference as noted above. It is interesting to note that the trends are very different when only the SMMR or the SSM/I data are used. Some differences are expected since the record lengths and the time periods are different. But part of the difference may have to do with the reduction and interpretation of the data. It should be noted that if one set of data (i.e., SSM/I) has a constant offset of 1% of the estimated extent, it would cause a change in trend of about 0.6%/decade. This is an important consideration since the Bootstrap and Team data show trends of 0.11±0.33%/decade and 1.25±0.40%/decade, respectively, while *Bjorgo et al.* (1997) shows a negative but insignificant trend.

5 Discussion and Conclusions

The true characteristics of the Antarctic sea ice cover have been studied using satellite high and medium resolution visible and infrared sensors as well as the relatively coarse resolution microwave sensors. The high-resolution data provide the details in both spatial and seasonal variability in the physical characteristics of the sea ice cover that enables an improved interpretation of sea ice products derived from passive microwave data. The large discrepancies in ice concentrations derived from the Bootstrap and Team Algorithms have also been evaluated through comparative analysis with results from high-resolution data. Both passive microwave algorithms show a good general overview of the sea ice cover and an inherent weakness to detect slush and shuga ice cover as was demonstrated during freeze-up in the Cosmonaut Sea (Fig. 3, Table 1). In large areas within the ice pack, especially in the Weddell Sea, Amundsen Sea, and Ross Sea regions (Figs. 13, 16, 17; Table 1), where the Bootstrap and Team algorithm results differ substantially, the OLS and Landsat data provide relatively high concentrations showing good agreement with those from the Bootstrap Algorithm. Because of the dominance of snow

covered thick ice in these areas, the lack of agreement with the Team Algorithm results is likely associated with layering and flooding that affects the polarization which is a key parameter utilized by the Team Algorithm.

The passive microwave ice concentration data, however, do not always provide the true ice concentration, especially in very active and predominantly new ice regions. Sea ice is a continuously evolving entitity that changes in thickness and physical properties and hence radiative characteristics. The emissivity of newly formed ice is similar to that of open water at the very early stages and gradually increase to that of thick ice at a later stage. Statistically, the tie points for 100% ice currently used by existing algorithms correspond to those of thick ice. The results in predominantly new ice areas are therefore slightly lower than the true ice concentrations as strictly defined. However, it should be pointed out that ice concentration products that follow the strict definition of ice concentration would have very limited value since within errors, the entire ice pack would be practically all 100% ice. The identification of locations of new ice, divergence, and polynya areas is important in polar process studies. An ice cover product that provides a means for quantifying these areas and interpretation of their effects would be more important. Fortuitously, the thickness of new ice increases proportionately with ice concentration and with heat (and salinity) fluxes between the ocean and the atmosphere. The reduction in ice concentration due to the presence of new ice enables the identification of the features in the ice pack and a more accurate characterization of the ice cover.

Enhancements in the algorithm that makes use of higher frequency channels that are more sensitive to new ice can be made. An enhanced Team algorithm that makes use of the 85 GHz data has been introduced to make estimates closer to the true ice concentration. The dual

polarized 37 GHz channel can also be used by the Bootstrap Algorithm, as was done in the Arctic region, to get the values in thin ice region closer to the true ice concentration. However, much of the valuable information about the ice cover, such as location and extents of polynyas and leads, would be lost in such a technique since the ice cover beyond the ice edge would be virtually 100% all over. An ice classification algorithm that makes use of multichannel data to detect the different ice regimes within the ice pack would be desirable as a complement of the ice concentration product. Such combination, used in tandem would enable a more extensive utilization of the data, especially for heat and salinity flux and mass balance studies.

Our results also indicate that satellite data provide the best means for monitoring the ice extent and actual ice area. It is, however, very important that trend analysis is done with great care, especially, when data from different sensors are used for different time periods. Even slight changes in resolution may cause significant changes in the trend values for ice extent. Overlap periods should at least include the summer but preferably one whole year, to enable intercalibration of the different sensors and ensure that ice extent and ice area are consistently derived.

ACKNOWLEDGMENTS. The authors wish to acknowledge the excellent programming support of Robert Gersten of SSAI and Will Manning of the University of Maryland, Baltimore County. Funding for this project was provided by the EOS-Aqua project and the Cryosphere Program at NASA Headquarters.

References:

Ackley, S.F., M. Lange, and P. Wadhams, Snow cover effects on the Antarctic sea ice thickness, *Sea Ice Properties and Processes*, ed. by S.F. Ackley and W.F. Weeks, CRREL Monograph 90-1, 300 pp., Cold Regions Research and Engineering Laboratory, Hanover, New Hampshire, 1990.

Allison, I., Antarctic sea ice growth and oceanic heat flux, *Sea Level, Ice and Climatic Change*, International Association of Hydrological Sciences, Guildfold, UK, pp. 161-170, 1981.

Bjorgo, E., O.M. Johannessen, and M.W. Miles, Analysis of merged SSMR-SSMI time series of Arctic and Antarctic sea ice parameters 1978-1995. *Geophys. Res. Lett.*, 24(4), 413-416, 1997.

Cavalieri, D. J., P. Gloersen, and W.J. Campbell, Determination of sea ice parameters from Nimbus 7 SSMR, *J. Geophys. Res., 89*(D4), 5355-5369, 1984.

Cavalieri, D.J., P. Gloersen, C. Parkinson, J. Comiso, and H.J. Zwally, Observed hemispheric asymmetry in global sea ice changes, *Science, 278*(7), 1104-1106,1997.

Comiso, J. C., Characteristics of winter sea ice from satellite multispectral microwave observations, *J. Geophys. Rev., 91*(C1), 975-994, 1986.

Comiso, J.C., Variability and trends in Antarctic surface temperatures from in

situ and satellite infrared measurements, *J. Climate*, *13*(10), 1674-1696, 2000.

Comiso, J. C., and H. J. Zwally, Antarctic Sea Ice Concentrations Inferred from Nimbus-5 ESMR and LANDSAT imagery, *J. Geophys. Res.*, *87*(C8), 5836-5844, 1982.

Comiso, J.C., and H.J. Zwally, Temperature Corrected Bootstrap Algorithm, IEEE IGARSS'97 Digest, Volume 3, 857-861, 1997.

Comiso, J. C., S. F. Ackley, and A. L. Gordon, Antarctic sea ice microwave signatures and their correlation with in situ ice observations, *J. Geophys. Res.*, *89*(C1), 662-672,1984.

Comiso, J. C., T. C. Grenfell, D. L. Bell, M. A. Lange, and S. F. Ackley, Passive Microwave In situ observations of winter Weddell sea ice, *J. Geophy. Res.*, *94*, 10891-10905, 1989.

Comiso, J.C, T.C. Grenfell, M. Lange, A. Lohanick, R. Moore, and P. Wadhams, Microwave remote sensing of the Southern Ocean Ice Cover, Chapter 12, *Microwave Remote Sensing of Sea Ice*, (ed. by Frank Carsey), Am. Geophys. Union, Washington, D.C., 243-259, 1992.

Comiso, J.C., D. Cavalieri, C. Parkinson, and P. Gloersen, Passive microwave algorithms for sea ice concentrations, *Remote Sensing of the Env.*, *60*(3), 357-384, 1997.

Eicken, H., M.A. Lange, and G.S. Diekmann, Spatial variability of sea-ice properties in the Northwestern Weddell Sea, *J. Geophys. Res.*, 96, 10603-10615, 1991.

Gordon, A. L., and J. C. Comiso, Polynyas in the Southern Ocean, *Scientific American, 256,* 90-97, 1988.

Grenfell, T.C, D.J. Cavalieri, J.C. Comiso, M.R. Drinkwater, R.G. Onstott, I. Rubinstein, K.

Steffen, I. Rubinstein, D.P. Winebrenner, "Microwave signatures of new and young ice," Chapter 14, *Microwave Remote Sensing of Sea Ice,* (ed. by Frank Carsey), American Geophysical Union, Washington, D.C., 291-301, 1992.

Grenfell, T.C., J.C. Comiso, M.A. Lange, H. Eicken, and M.R. Wenshahan, Passive microwave observations of the Weddell Sea during austral winter and early spring, *J. Geophys, Res., 99*(C5), 9995-10,010, 1994.

Hall, R.T., AIDJEX modeling group studies involving remote sensing data; *Sea Ice Processes and Models,* ed. R.S. Pitchard, 151-162, University of Washington Press, Seattle, 1980.

Ito, H., Decay of the sea ice in the North Water area: Observation of ice cover in Landsat images, *J. Geophys. Res., 90*, 8102-8110, 1985.

Jacobs, S.S, and J.C. Comiso, A recent sea-ice retreat west of the Antarctic Peninsula, *Geophys. Res. Letter, 20*(12), 1171-1174, 1993.

Kwok R., A. Schweiger, D.A. Rothrock, S. Pang, and C. Kottmeier, Sea ice motion from satellite passive microwave imagery assessed with ERS SAR and buoy motions, *J. Geophys. Res.*, 103(C4), 8191-8214, 1998.

Lange, M., H. Eicken, and M.R. Wenshahan, Passive microwave observations of the Weddell Sea during austral winter and early spring, *J. Geophys, Res., 99*(C5), 9995-10,010, 1994.

Markus, T., and D. Cavalieri , An enhancement of the NASA Team Algorithm, *IEEE Trans. on*

Geoscience and Remote Sensing, 38(3), 1387-1298, 2000.

Massom, R.A., J.C. Comiso, A.P. Worby, V. Lytle, and L. Stock, Satellite and in situ observations of regional classes of sea ice cover in the East Antarctic pack in winter, *Remote Sensing of the Env.*, *68*(1), 61-76, 1999.

Mätzler, C., R.O. Ramseier, and E. Svendsen, Polarization effects in sea ice signatures, *IEEE J. Oceanic Eng. OE-9,* 33-338, 1984.

Maykut, G. A., Energy exchange over young sea ice in the Central Arctic, *J. Geophy. Res.*, *83*(C7), 3646-3658, 1978.

Parkinson, C. L., J. C. Comiso, H. J. Zwally, D. J. Cavalieri, P. Gloersen, and W. J. Campbell, Arctic Sea Ice 1973-1976 from Satellite Passive Microwave Observations, *NASA Spec. Publ. 489*, 1987.

Rothrock, D. A., Y. Yu, and G. A. Maykut, Thinning of the Arctic sea-ice cover, *Geophys. Res. Letters*, 26(23), 3469-3472, 1999.

Steffen, K., Atlas of sea ice types, deformation processes and openings in the ice, *Zürcher Geographische Schriften, 20*, p. 55, 1986.

Steffen, K., Energy flux density estimation over sea ice based on satellite passive microwave measurements, *Ann. Glaciology, 15,* 178-183, 1991.

Steffen, K., and A. Schweiger. NASA team algorithm for sea ice concentration retrieval from

Defense Meteorological Satellite Program special sensor microwave imager: comparison with Landsat satellite data, *J. Geophys. Res.*, 96(C12), 21,971-21,987, 1991.

Steffen, K., D. J. Cavalieri, J. C. Comiso, K. St. Germain, P. Gloersen, J. Key, and I. Rubinstein, "The estimation of geophysical parameters using Passive Microwave Algorithms," Chapter 10, *Microwave Remote Sensing of Sea Ice,* (ed. by Frank Carsey), American Geophysical Union, Washington, D.C., 201-231, 1992.

Tucker III, W.B., D.K. Perovich, A.J. Gow, W.F. Weeks, and M.R. Drinkwater, Physical properties of sea ice relevant to remote sensing, Chapter 2, *Microwave Remote Sensing of Sea Ice,* (ed. by Frank Carsey), American Geophysical Union, Washington, D.C., 201-231, 1992.

Weeks, W.F., and S.F. Ackley, The growth, structure, and properties of sea ice, *The Geophysics of Sea Ice*, ed. by N. Unterstiener, pp. 9-164, NATO ASI Series B: Physics vol. 146, Plenum Press, New York, 1986.

Zwally, H. J., J. C. Comiso, C. L. Parkinson, W. J. Campbell, F. D. Carsey, and P. Gloersen, Antarctic Sea Ice 1973-1976 from Satellite Passive Microwave Observations, *NASA Spec. Publ. 459*, 1983.

List of Figures:

1. Aircraft photographs of (a) grease ice; (b) Gray ice with flooding from wave interaction; (c) pancake ice and finger rafting;(d) finger rafting with frost and salt flowers; (e) ridged ice; and (f) gray and gray-white ice with refrozen lead.

2. Helicopter photograph of a typical Antarctic sea ice cover within the ice pack in September 1989 during the Weddell Gyre Experiment, showing ridges, flooded surfaces, and RV Polarstern in a lead area.

3. Antarctic map showing the seven locations of Landsat and SSM/I intercomparison.

4. Landsat TM image from Cape Ann and Cape Batterbee region, March 27, 1989 The image depicts a slush and shuga ice cover in (a), whereas, the sub-scene shows wind and wave interaction with suga ice cover and ice bergs (b). NCEP 500 hPa geopotential height (e.g., 570 x 10 m)(c), and NCEP surface temperature in degree Kelvin (d) are shown for the same data the Landsat scene was acquired.

5. Landsat TM image, Cape Batterbee and Magnet Bay, November 24, 1989, with compact pack ice in a matrix of gray ice and nilas (a); numerous ice bergs frozen in fast ice of the magnet Bay (b), large dark surface area of Cape Batterbee represents a nilas ice cover (c), and sub-scene of large ice floes showing digital enhanced surface structure of refrozen conglomerate of different ice floes (d).

6. Monthly average of cloud free AVHRR Channel 1 (0.6 μm) GAC data in the last weeks of (a) March 1989, and (b) November 1989, and SSM/I data in the last weeks of (c) March 1989

and (d) November 1989.

7. Ice concentration and difference maps in ice concentration using Team and Bootstrap techniques for July, August, September and October 1992.

8. Brightness temperature maps of the Antarctic region on September 30, 1992 at 6 SSM/I frequencies and polarizations.

9. Brightness temperatures for all SSM/I channels and ice concentration along the 33° Longitude (indicate by white or black line in Fig. 8). The vertical dotted line indicates the approximate location of the ice edge where the ice concentration is 15 to 20%.

10. Scatter Plots of (a) 19 GHz (V) versus 37 GHz (V); (b) Gradient versus polarization ratio using data on September 30, 1992. The green, red, and yellow dots are from box 1, 2, and 3, respectively shown in Figure 11. (c) Frequency histogram of ice concentrations in the Antarctic using the Bootstrap (solid thick) and Team (solid thin) algorithms.

11. (a) OLS visible data on September 30, 1992 and location of study areas; (b) Classified OLS image in Box 1, 2, and 3; (c) Bootstrap ice concentrations over the same general area as (a) with the study areas identified; and (d) Team ice concentration over the same general area as (a) with study areas identified.

12. (a) OLS visible data on October 7, 1992 and location of 2 study areas; (b) Classified OLS data in boxes 1 and 2; (c Bootstrap ice concentrations over the same general area as (a) with study areas identified; (d) Team ice concentrations over the same general area as (a) with study areas identified.

13. (a) Passive microwave-derived ice concentration (Bootstrap algorithm) on September 18, 1988; (b) Ice concentration map derived using the Landsat image, NASA Team, and Bootstrap algorithm (color code for ice concentration is given in (a)) for the same day with the location of the Landsat image in (a) identified by a box; and (c) ice concentration derived using themaximum likelihood classifier with Landsat MSS channel 4. The box in (c) is enlarged on the right to show the small amount of open water in leads.

14. Comparison of OLS, Bootstrap, and Team data in the Ross Sea on September 1, 1995.

15. Landsat TM comparison for the Ross Sea, December 16, 1988; (a) TM channels 2, 3 4 as color composite blue-red-green image; (b) Landsat ice concentration with mean value of 89.2%, (c) Team Algorithm ice concentration with mean value of 83.8%, and (d) Bootstrap ice concentration with mean value of 89.2% for each 25 km x 25 km pixel according to the color code.

16. Landsat MSS comparison for the Amundsen Sea, December 1990. This Landsat image was classified using channel 4 for ice typing (a) using the threshold method, and channel 2 and 4 for cloud detection. The color-coded classified scene depicts an average ice concentration of 85% for the Landsat scene (lower panel). The passive microwave derived ice concentrations were 83% for the Team algorithm, and 90% for the Bootstrap algorithm, respectively.

17. Landsat TM data in the Bellinghausen Sea on December 15, 1988. Most of the dark regions shown on this image are regions covered with black nilas which can be detected with a

digitally stretched image. The resulting mean ice concentrations are 92%, 84%, and 94% for Landsat, Team, and Boostrap algorithms, respectively.

18. Landsat TM scene in the western Pacific Ocean on November 17, 1989. Large areas are covered with brash ice, gray ice and shuga, resulting in ice concentrations of 73%, 51%, and 70%, respectively, for the Landsat, Team, and Bootstrap algorithms.

19. (a) Surface temperature maps for September 1992; and (b) Ice concentration maps using the data in (a) and a temperature corrected algorithm and (c) difference map of (b) and (a).

20. (a) AVHRR LAC image of the Ross Sea on May 22, 1995; and (b) ice concentration from SSM/I data using the Bootstrap Algorithm on May 22, 1995.

21. Ice vectors in the Ross Sea and Amundsen Sea region derived using time series of passive microwave data for the periods (a) March to April 1992; (b) May to June 1992; (c) July to August, 1992; and (c) September to October 1992. The vectors show strong ice advections adjacent to the Ross Shelf. (Plot provided by R. Kwok, Jet Propulsion Laboratory).

22. Plots of (a) annual Antarctic sea ice extents derived from the Bootstrap (upper curve) and Team (lower curve) algorithms; and (b) difference between Bootstrap and Team values.

23. Plots of monthly anomalies in (a) ice extent; (b) actual ice area; and (c) ice concentration from 1978 through 2000 derived using Bootstrap algorithm ice concentration data.

Table 1: Landsat MSS and TM scenes used in the ice concentration (L) comparison with SSM/I derived values from the Team Algorithm (T) and Boot Strap Algorithm (B). The locations of the Landsat scenes are shown in Figure 3.

Scene	Fig.	Date	Sensor	Ice conc. (%) L / T / B	Ice conditions
1	4	Mar 27, 1989	TM	72 / 40 / 50	slush, shuga and pancake ice
2	5	Nov 24, 1989	TM	99 / 82 / 91	white ice floes with nilas and gray ice
3	18	Nov 17, 1989	TM	73 / 51 / 70	white ice floes, young ice, nilas and gray ice
4	15	Dec 16, 1988	TM	89 / 73 / 84 /	white ice with shuga along the ice edge and open water
5	16	Dec 29, 1990	MSS	85 / 83 / 90	white ice floes of varying size
6	17	Dec 15, 1988	TM	92 / 84 / 94	white ice, gray ice, nilas, and open water
7	13	Sept 18, 1988	MSS	100 /65 / 100	white ice, gray ice and trace of open water in a few leads

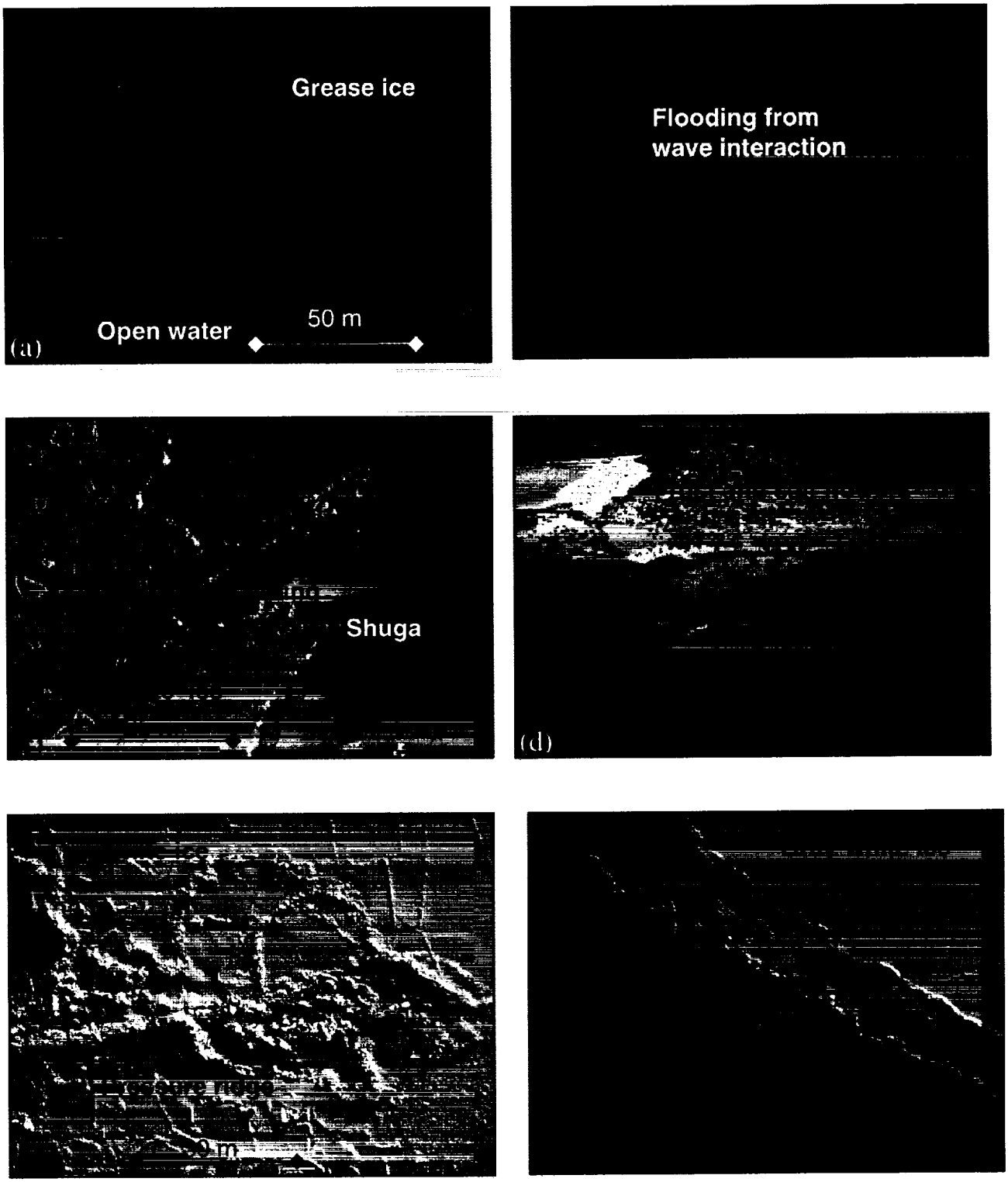
Grease ice
Open water
50 m
(a)
Flooding from
wave interaction
Shuga
(d)

Fig 1

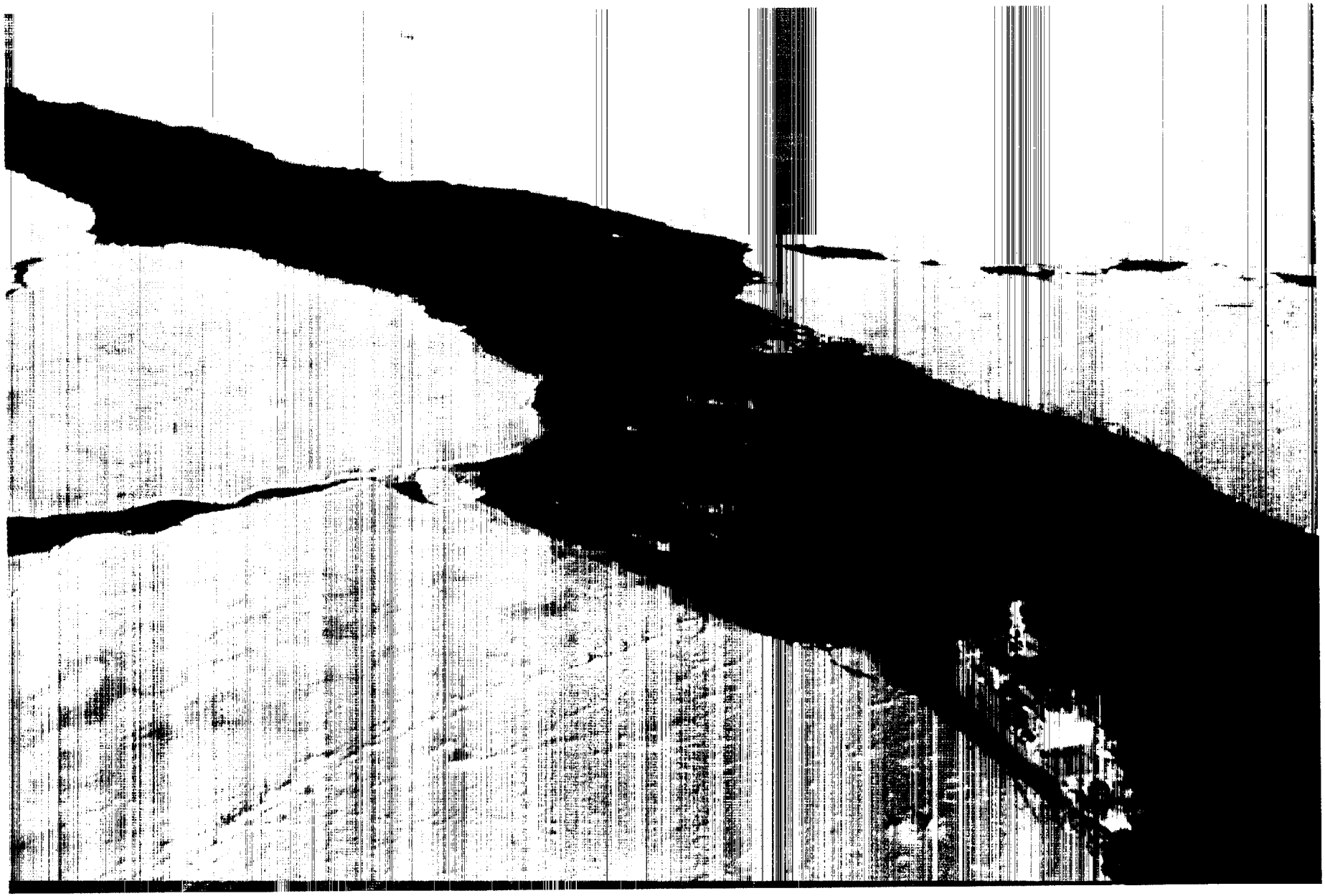

Fig. 2

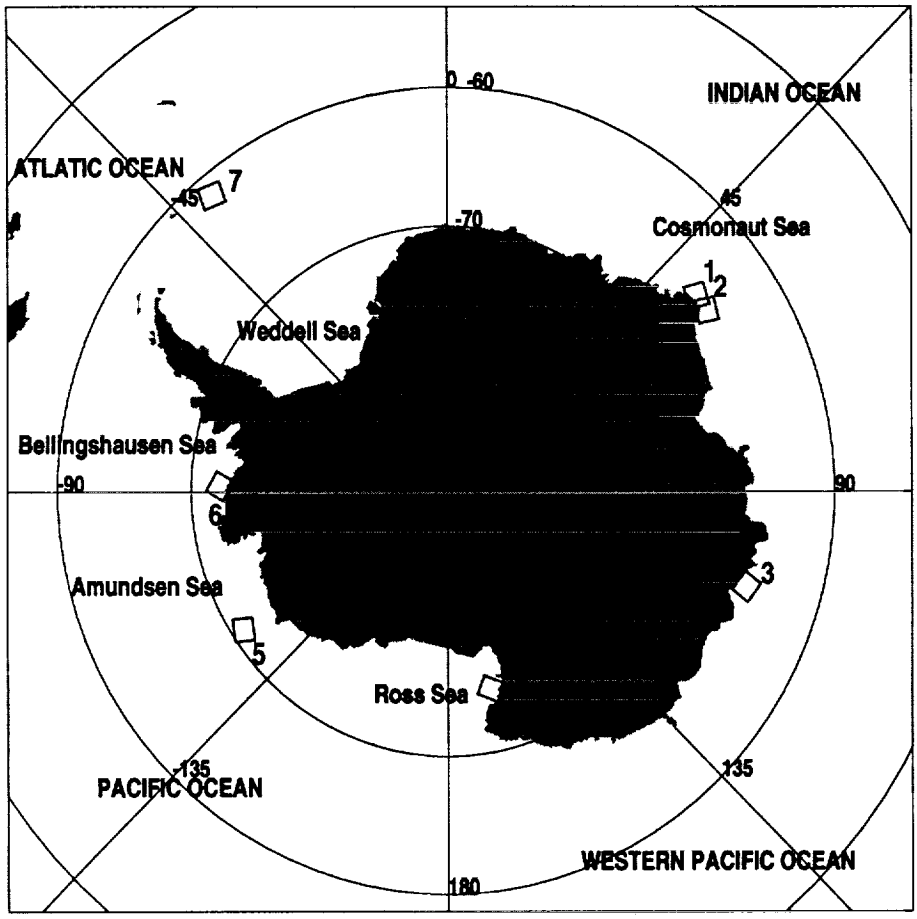
0 -60
INDIAN OCEAN
ATLATIC OCEAN
-45
7
45
-70
Cosmonaut Sea
1
2
Weddell Sea
Bellingshausen Sea
-90
90
6
3
Amundsen Sea
5
Ross Sea
-135
135
PACIFIC OCEAN
WESTERN PACIFIC OCEAN
180

Fig. 3

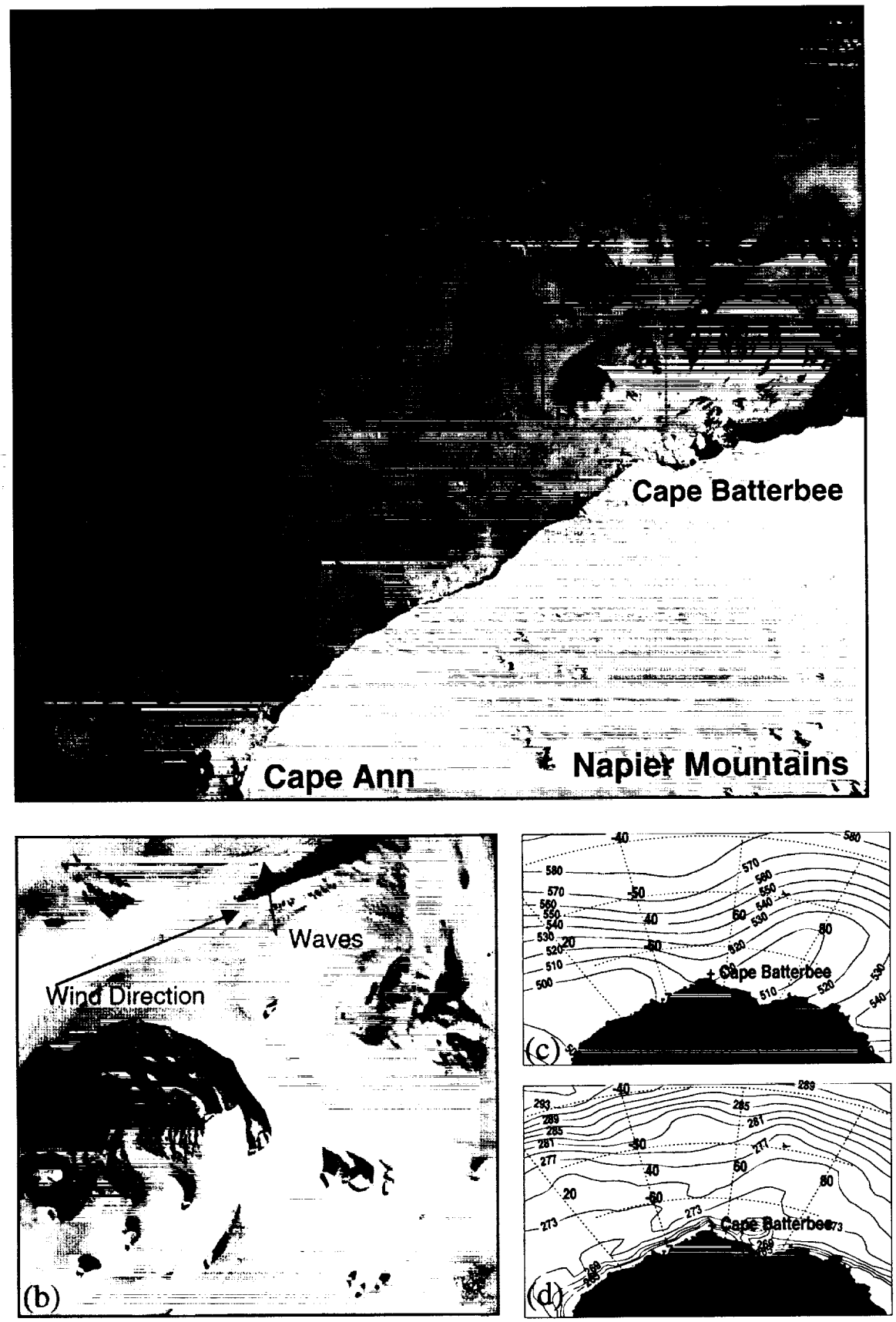
Cape Batterbee
Cape Ann
Napier Mountains
Waves
Wind Direction
(b)
Cape Batterbee
(c)
Cape Batterbee
(d)

Figure 4:

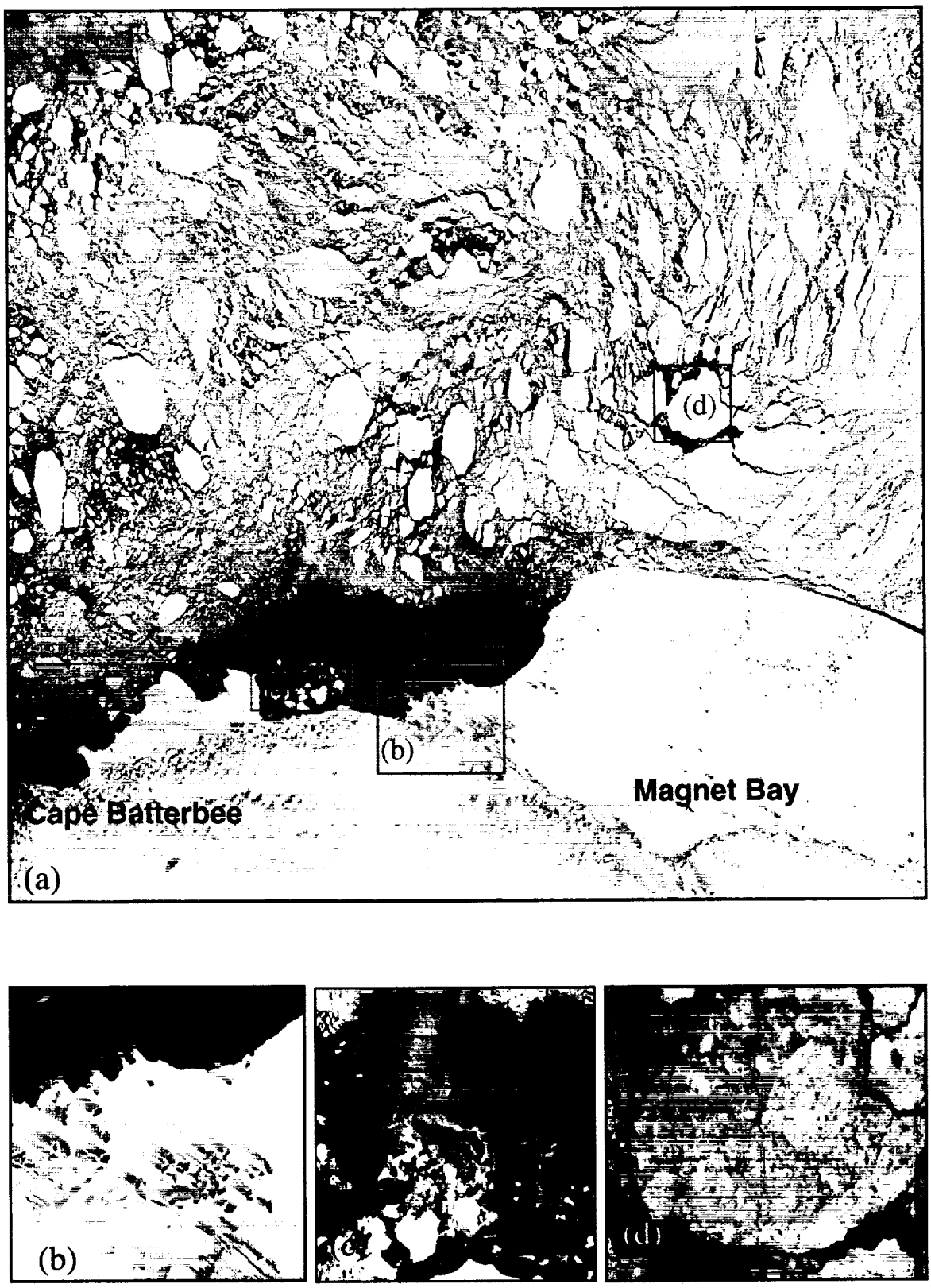

Figure 5

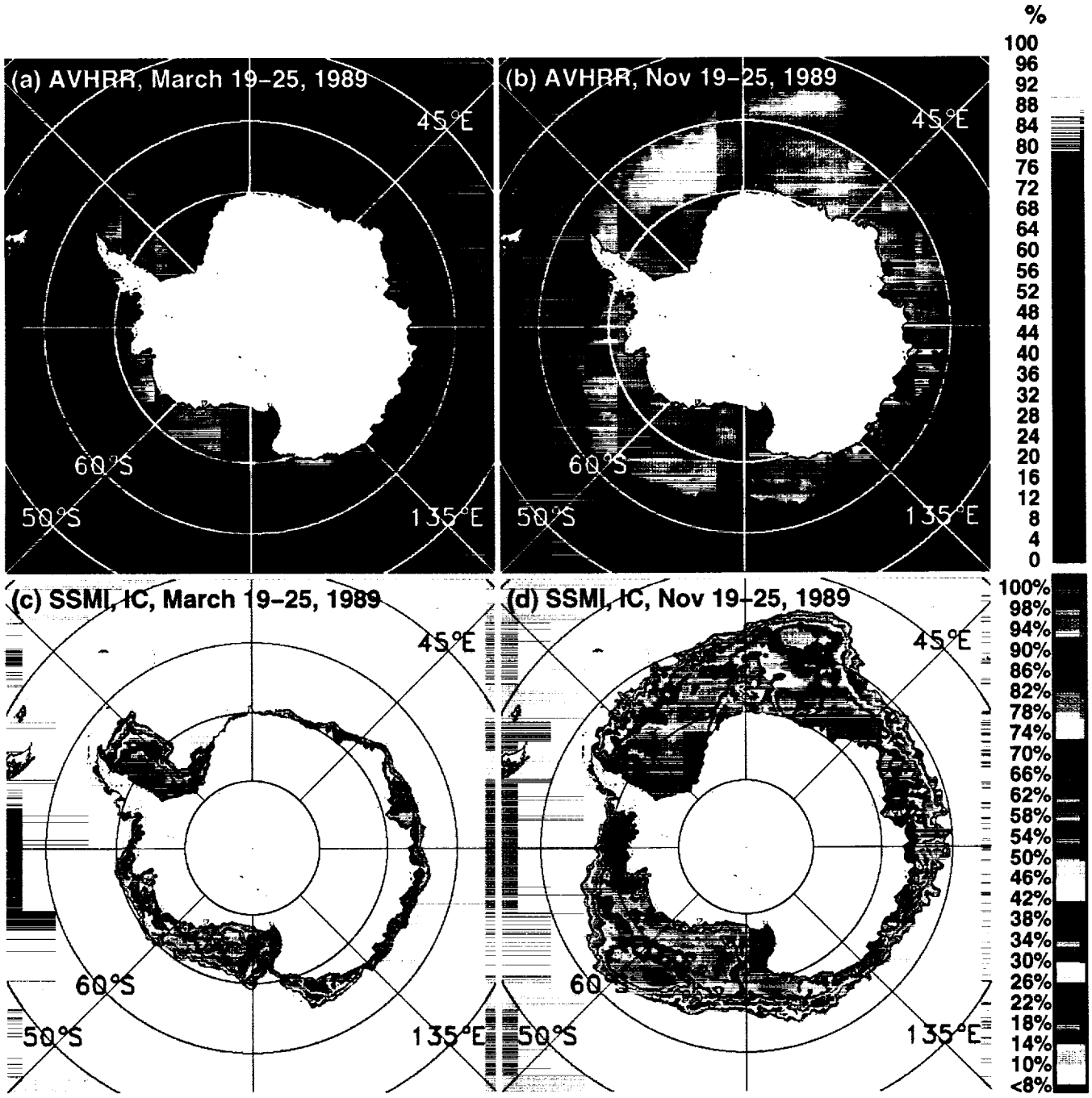
(a) AVHRR, March 19–25, 1989
(b) AVHRR, Nov 19–25, 1989
(c) SSMI, IC, March 19–25, 1989
(d) SSMI, IC, Nov 19–25, 1989
45°E
135°E
60°S
50°S
%
100
96
92
88
84
80
76
72
68
64
60
56
52
48
44
40
36
32
28
24
20
16
12
8
4
0
100%
98%
94%
90%
86%
82%
78%
74%
70%
66%
62%
58%
54%
50%
46%
42%
38%
34%
30%
26%
22%
18%
14%
10%
<8%

Fig. 6

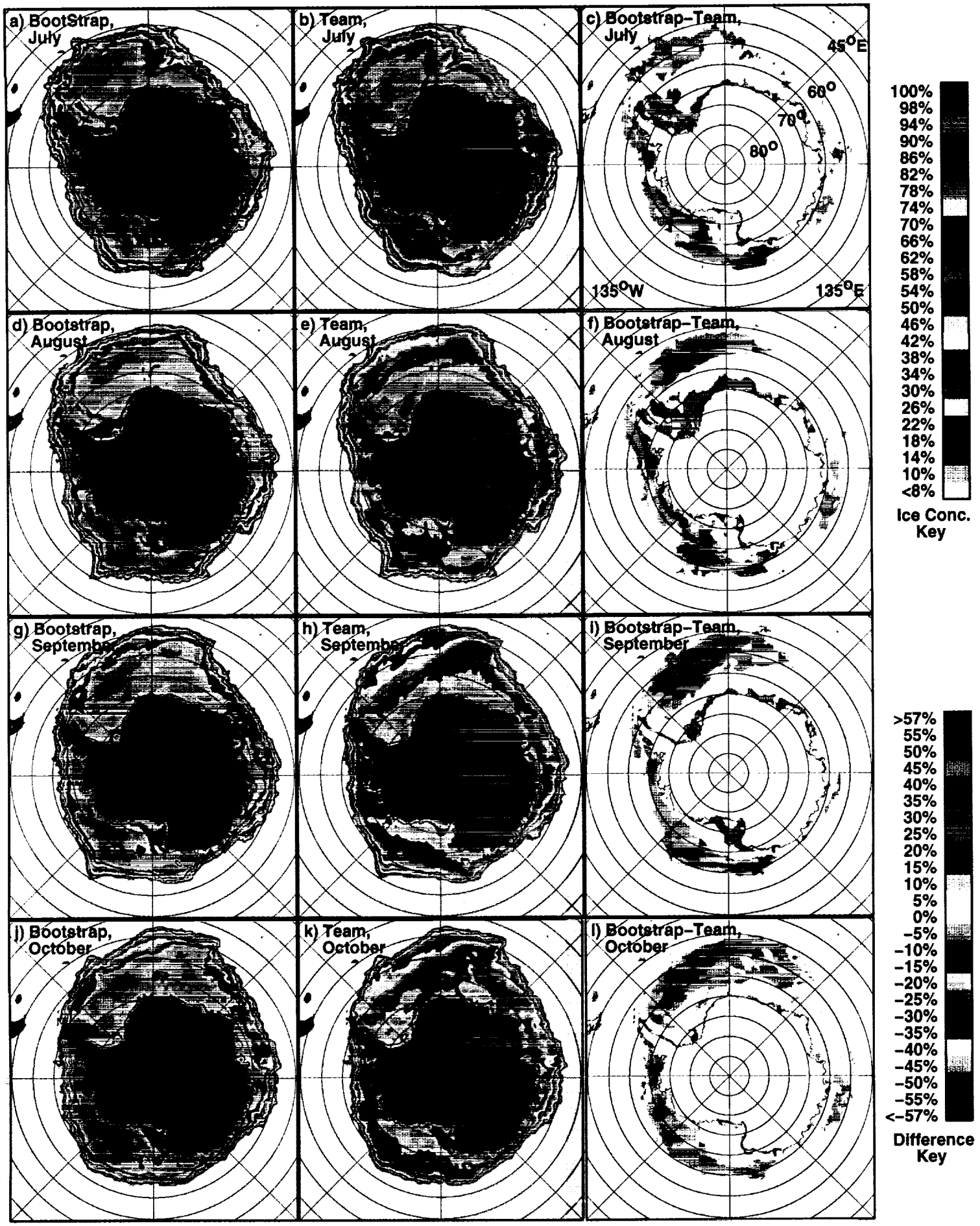
a) BootStrap, July
b) Team, July
c) Bootstrap–Team, July
45°E
60°
70°
80°
135°W
135°E
d) Bootstrap, August
e) Team, August
f) Bootstrap–Team, August
g) Bootstrap, September
h) Team, September
i) Bootstrap–Team, September
j) Bootstrap, October
k) Team, October
l) Bootstrap–Team, October
100%
98%
94%
90%
86%
82%
78%
74%
70%
66%
62%
58%
54%
50%
46%
42%
38%
34%
30%
26%
22%
18%
14%
10%
<8%
Ice Conc. Key
>57%
55%
50%
45%
40%
35%
30%
25%
20%
15%
10%
5%
0%
-5%
-10%
-15%
-20%
-25%
-30%
-35%
-40%
-45%
-50%
-55%
<-57%
Difference Key

Fig. 7

September 30, 1992

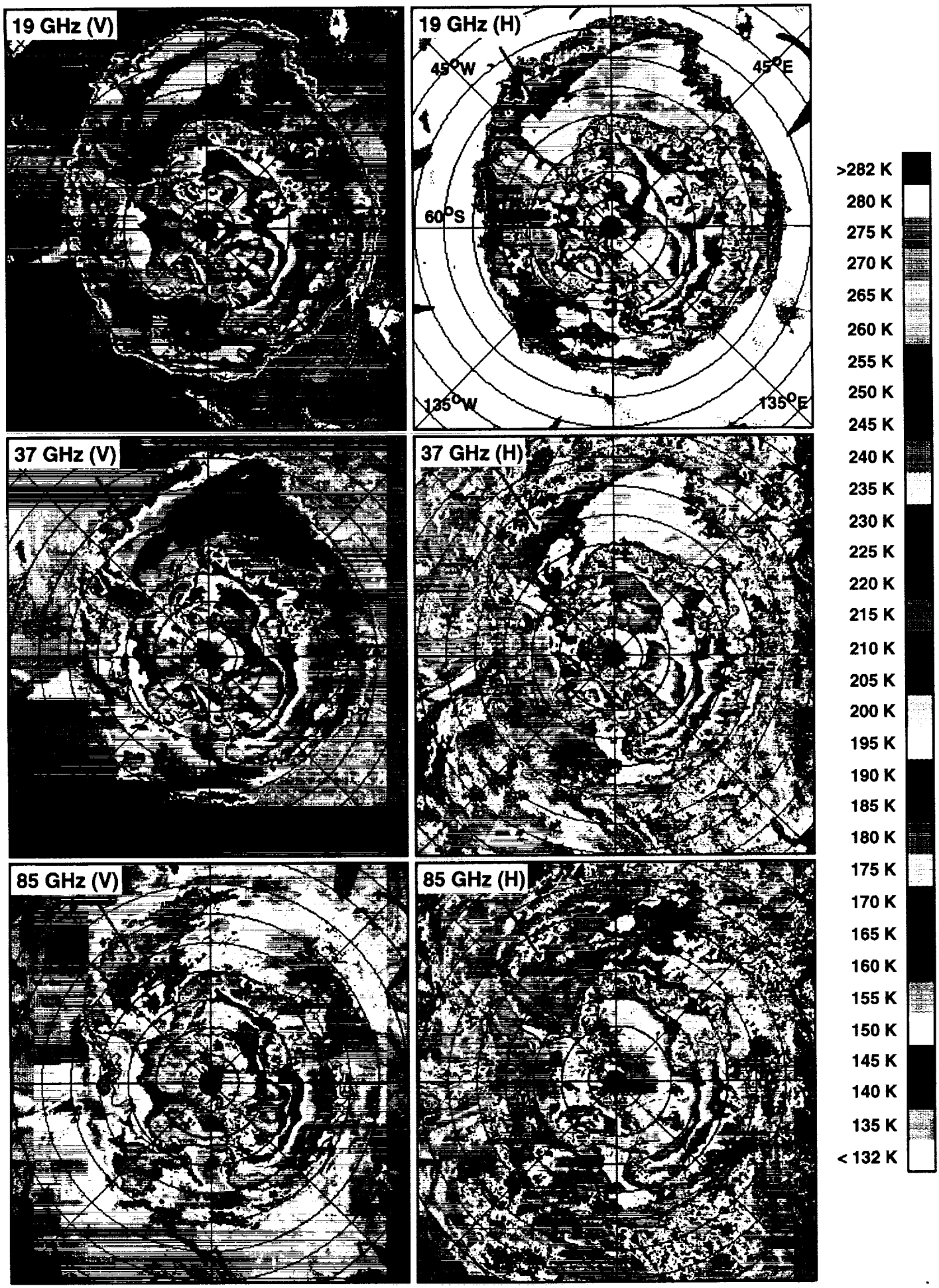

Fig. 8

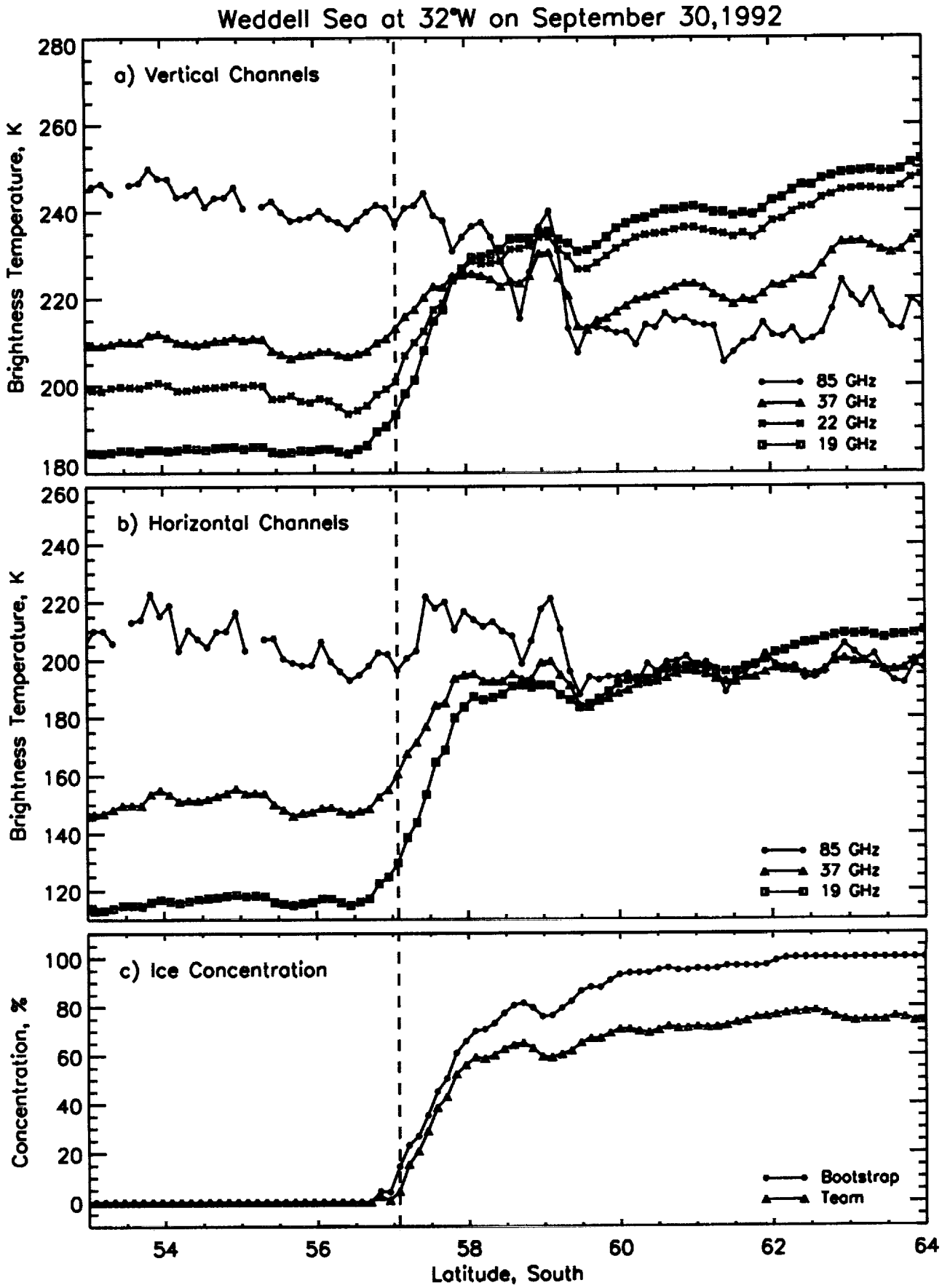
Weddell Sea at 32°W on September 30,1992
a) Vertical Channels
Brightness Temperature, K
85 GHz
37 GHz
22 GHz
19 GHz
b) Horizontal Channels
Brightness Temperature, K
85 GHz
37 GHz
19 GHz
c) Ice Concentration
Concentration, %
Bootstrap
Team
Latitude, South

Fig.9

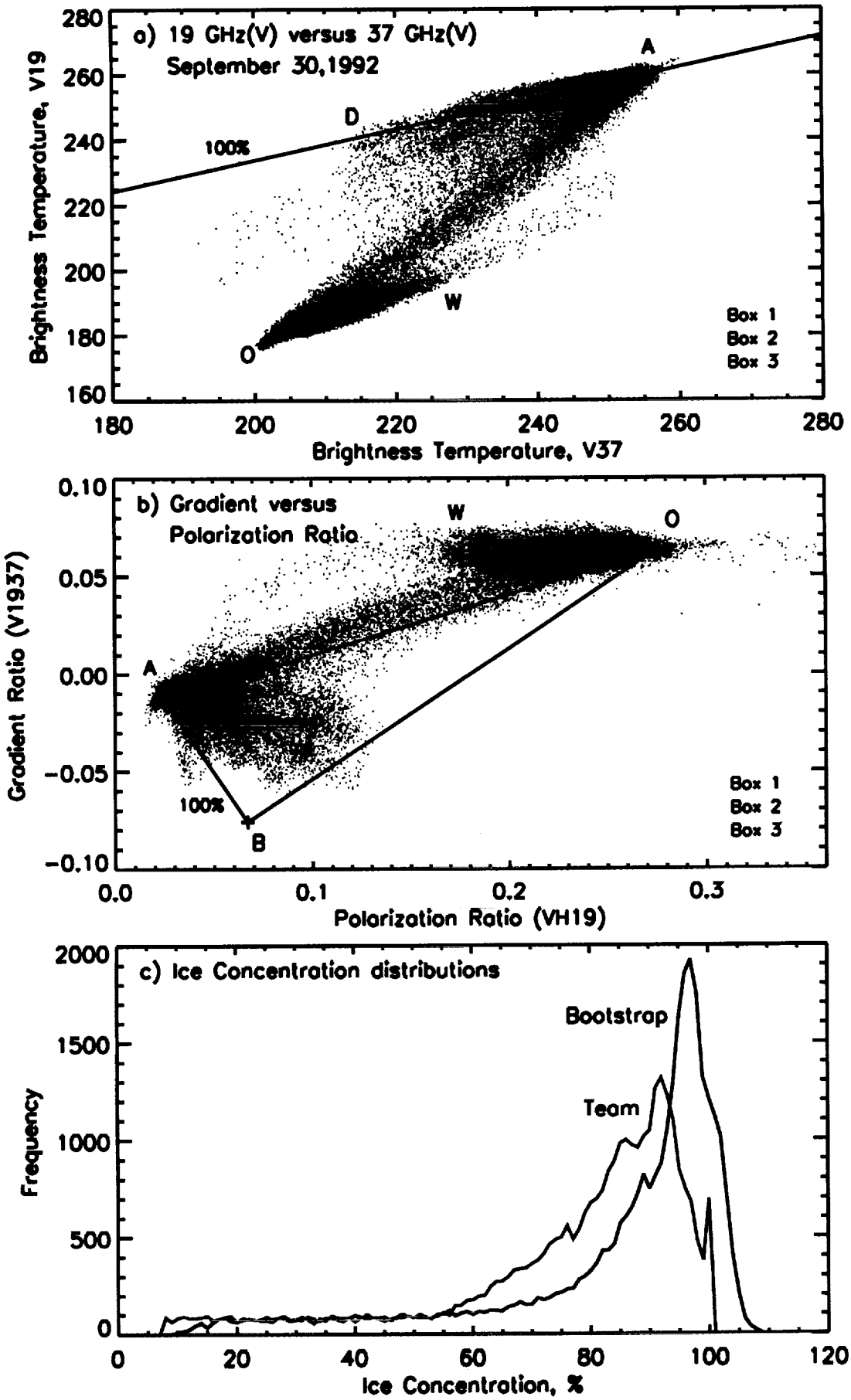
a) 19 GHz(V) versus 37 GHz(V)
September 30,1992
A
D
100%
W
O
Box 1
Box 2
Box 3
Brightness Temperature, V19
Brightness Temperature, V37
b) Gradient versus
Polarization Ratio
W
O
A
100%
B
Box 1
Box 2
Box 3
Gradient Ratio (V1937)
Polarization Ratio (VH19)
c) Ice Concentration distributions
Bootstrap
Team
Frequency
Ice Concentration, %

Fig. 10

September 30, 1992

a) OLS Visible

b) OLS IC

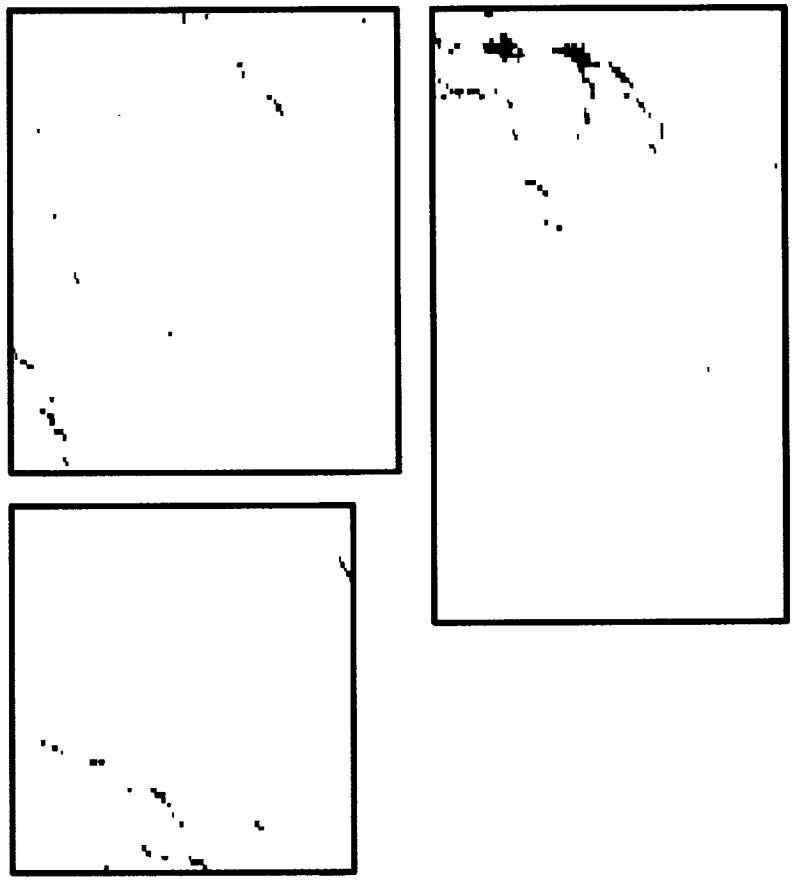

c) Bootstrap IC

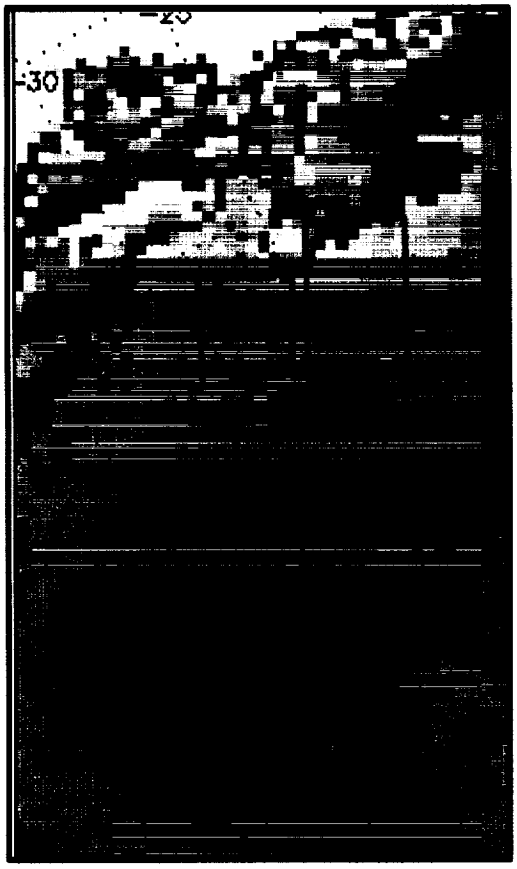

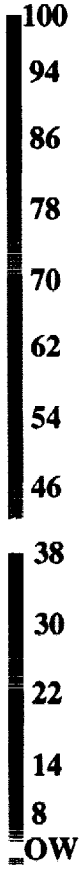

d) Team IC

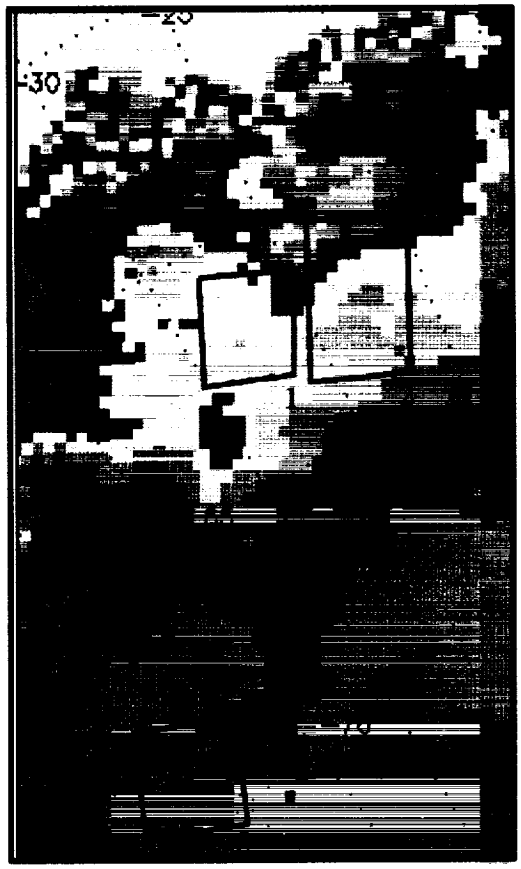

Fig 11

October 7, 1992

a) OLS Visible

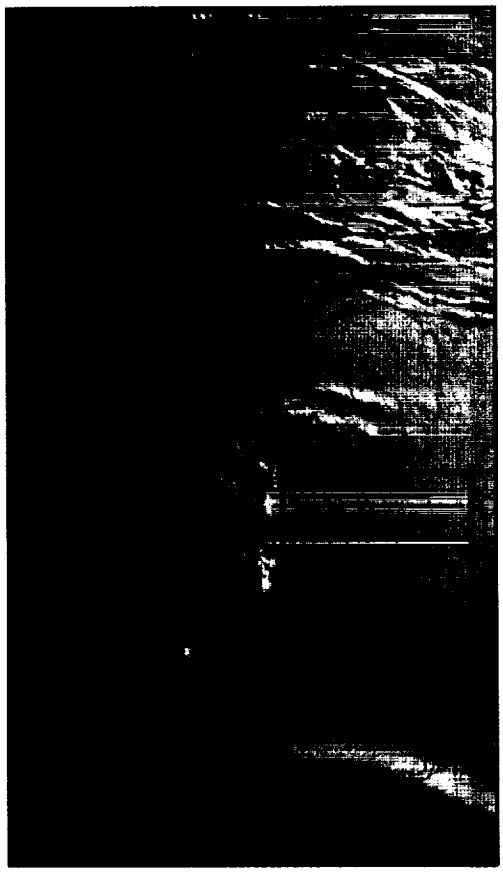

b) OLS IC

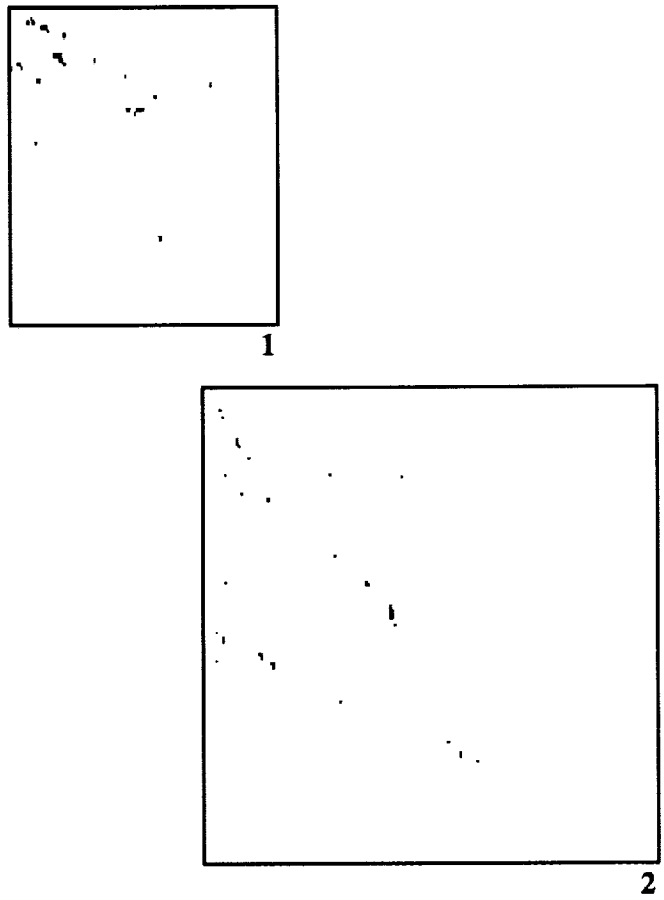

c) Bootstrap IC

d) Team IC

Fig 12

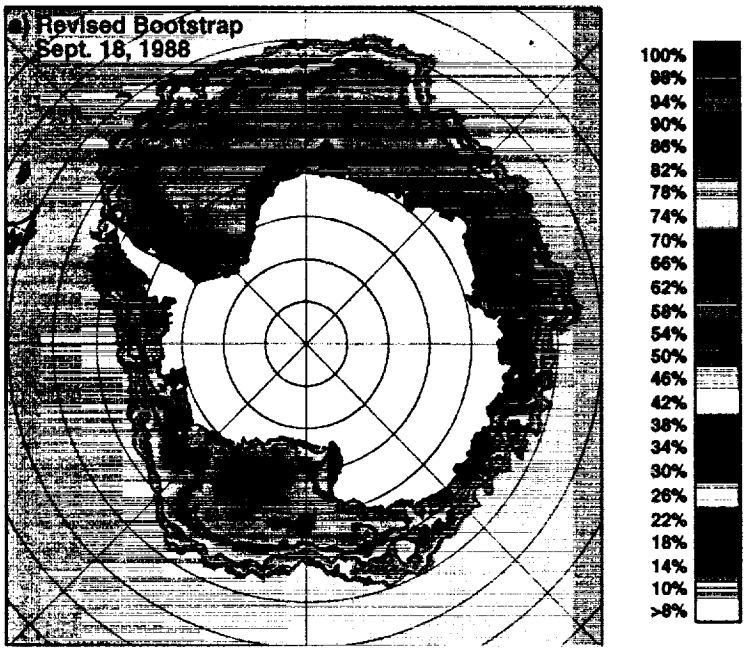
Revised Bootstrap
Sept. 18, 1988
100%
98%
94%
90%
86%
82%
78%
74%
70%
66%
62%
58%
54%
50%
46%
42%
38%
34%
30%
26%
22%
18%
14%
10%
>8%

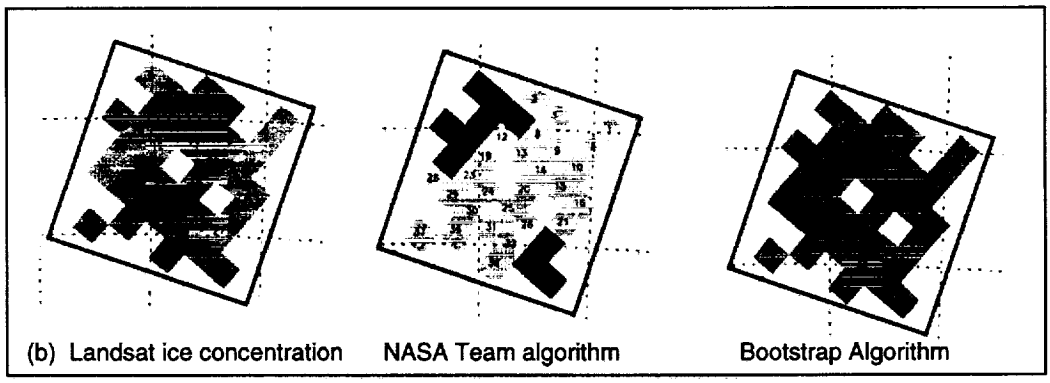
(b) Landsat ice concentration
NASA Team algorithm
Bootstrap Algorithm

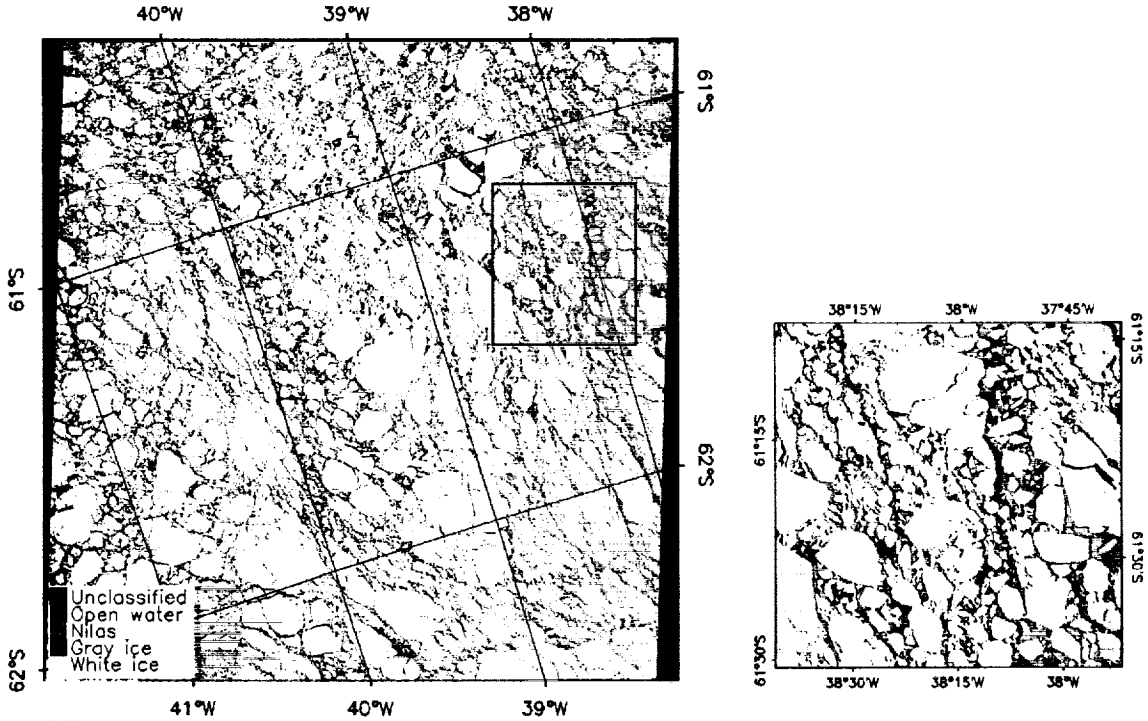
40°W
39°W
38°W
61°S
62°S
Unclassified
Open water
Nilas
Gray ice
White ice
41°W
40°W
39°W
38°15'W
38°W
37°45'W
61°15'S
61°30'S
38°30'W
38°15'W
38°W

(c)

Figure 13

September 1, 1995

OLS Visible

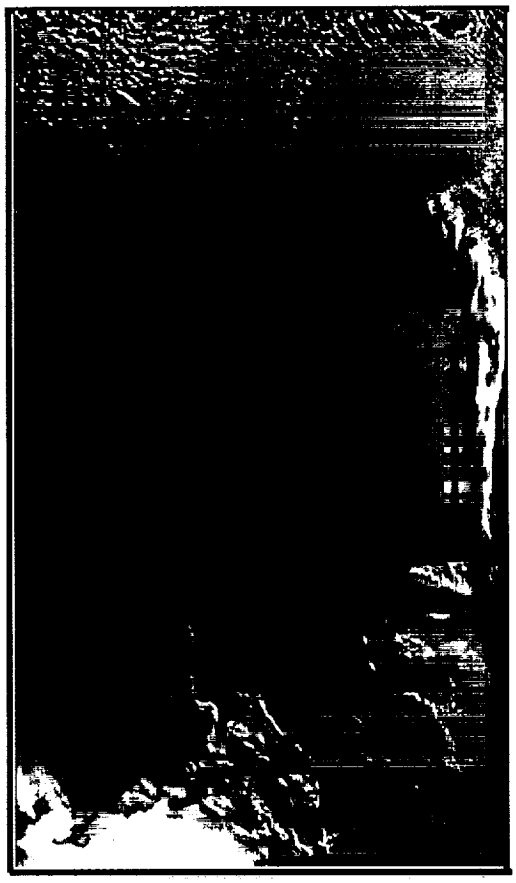

OLS IC = 98.9%

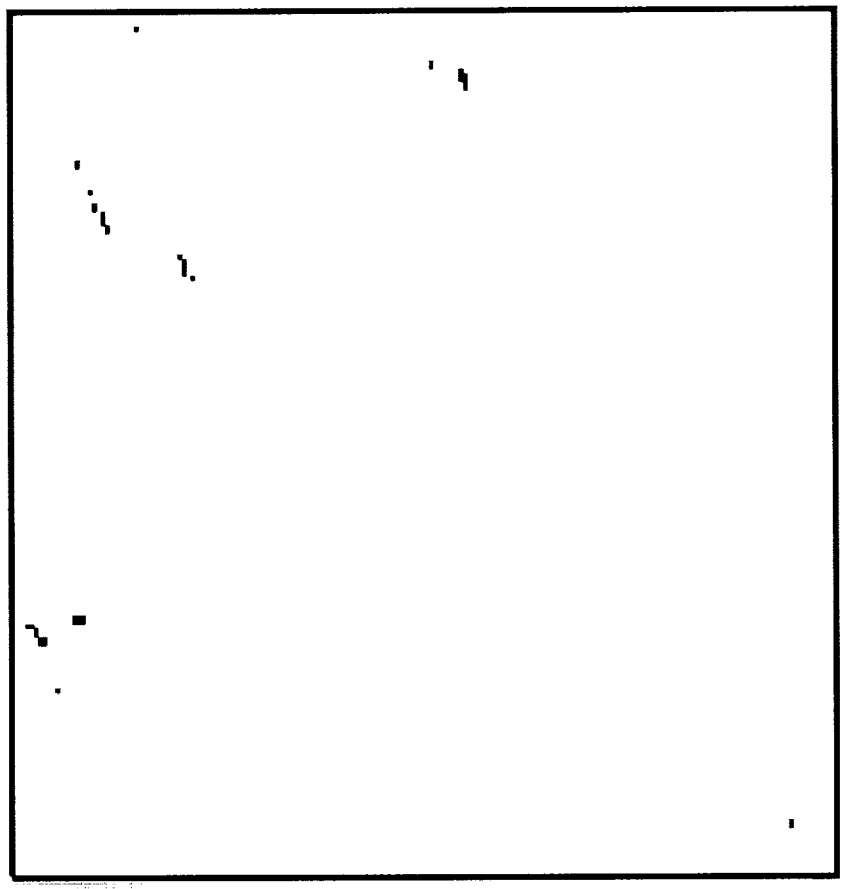

Bootstrap IC = 95.0%

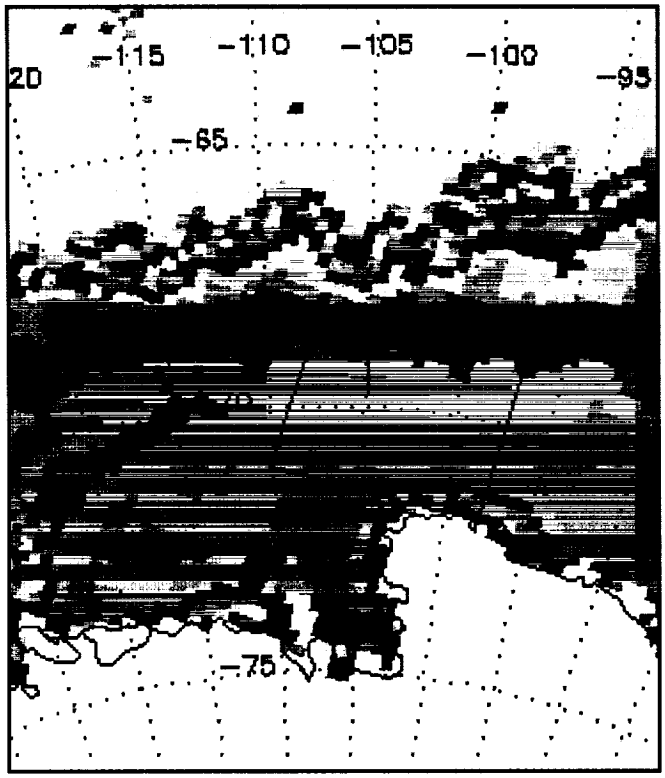

Team IC = 79.1%

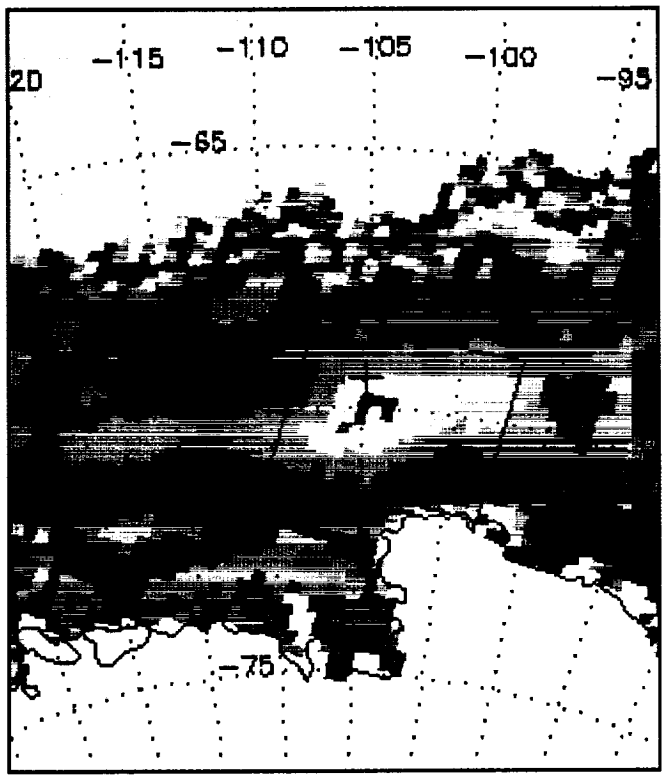

Fig 14

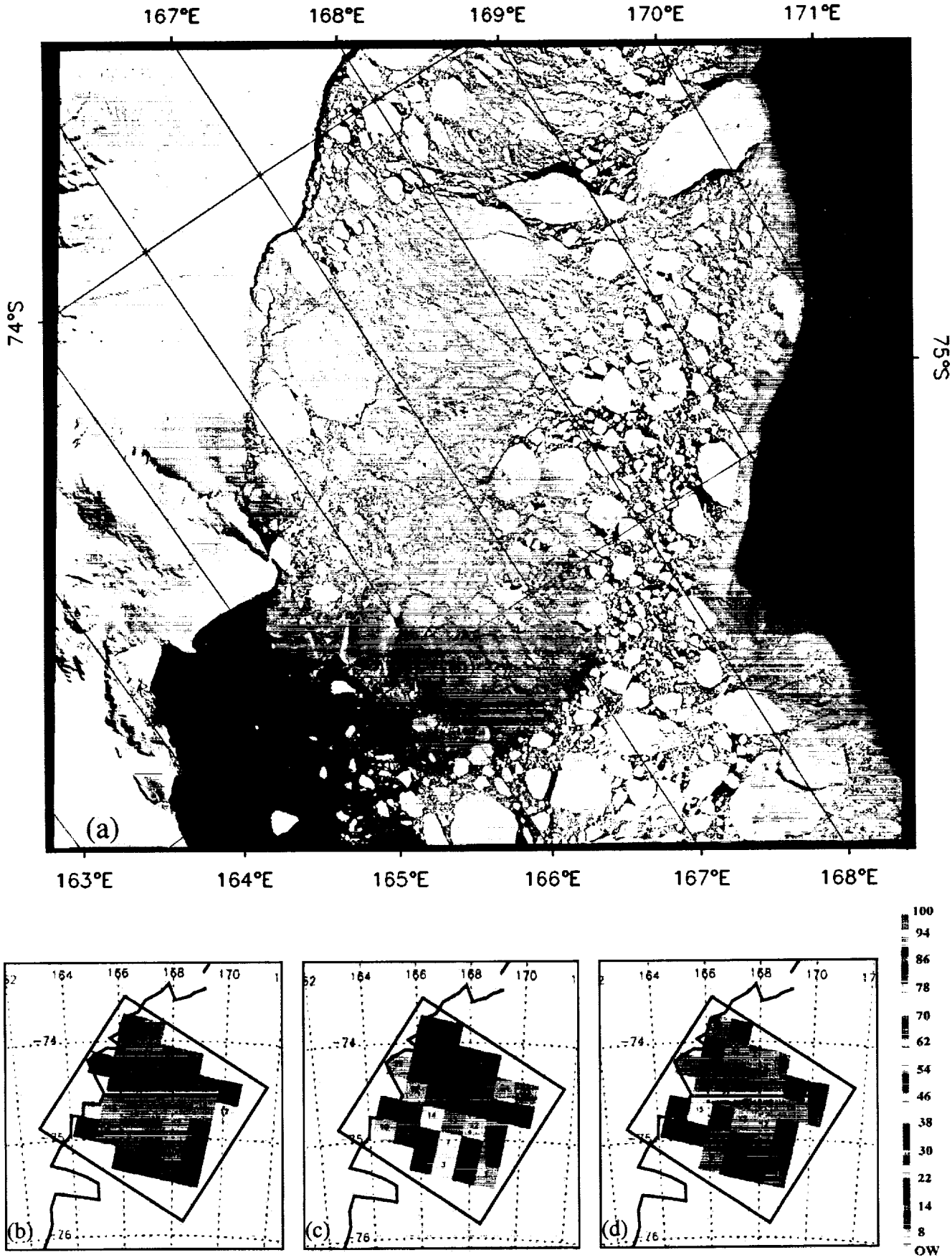

Figure1 15: : Ross Sea, December 16, 1988

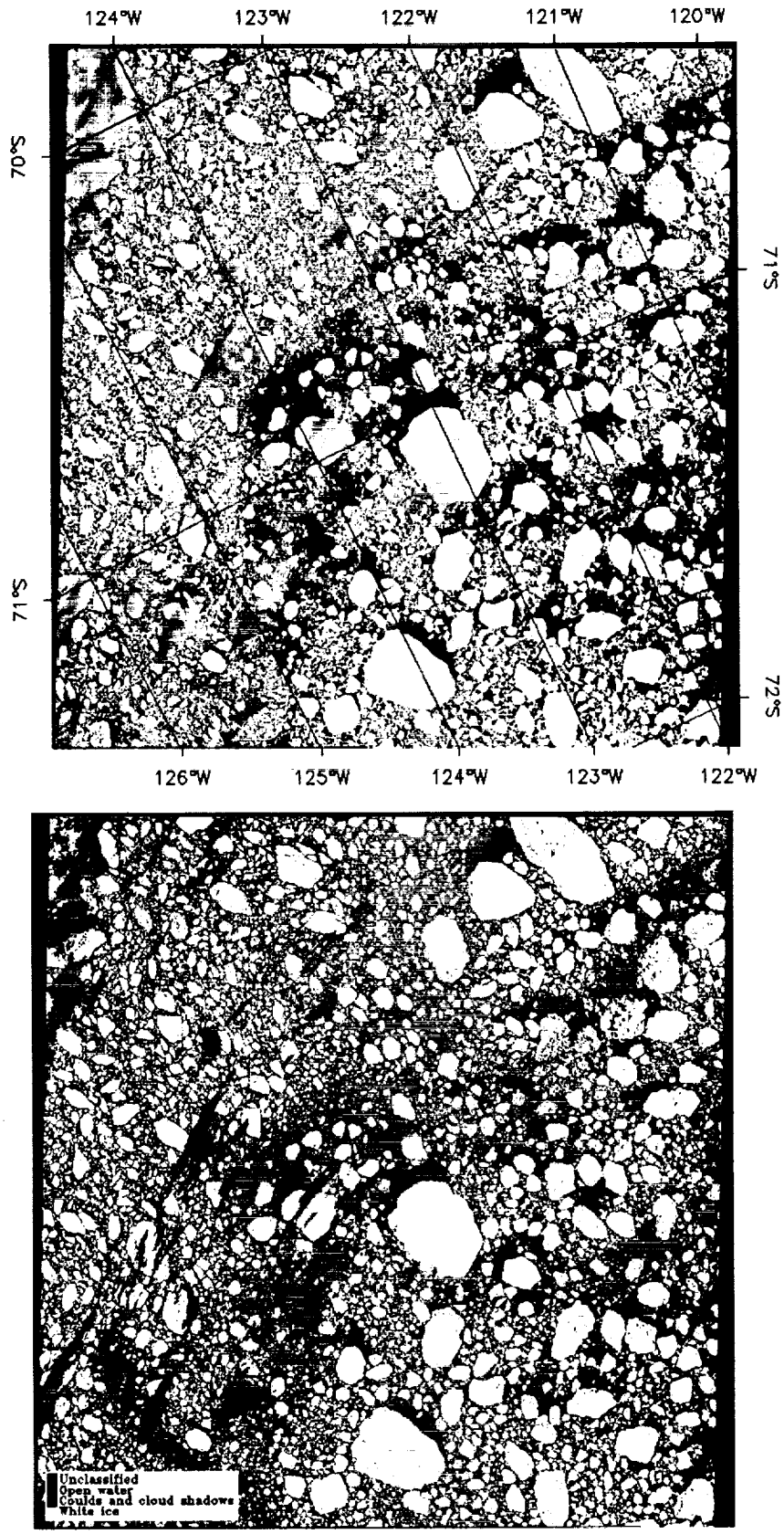

Fig. 16: Dec. 29, 1990

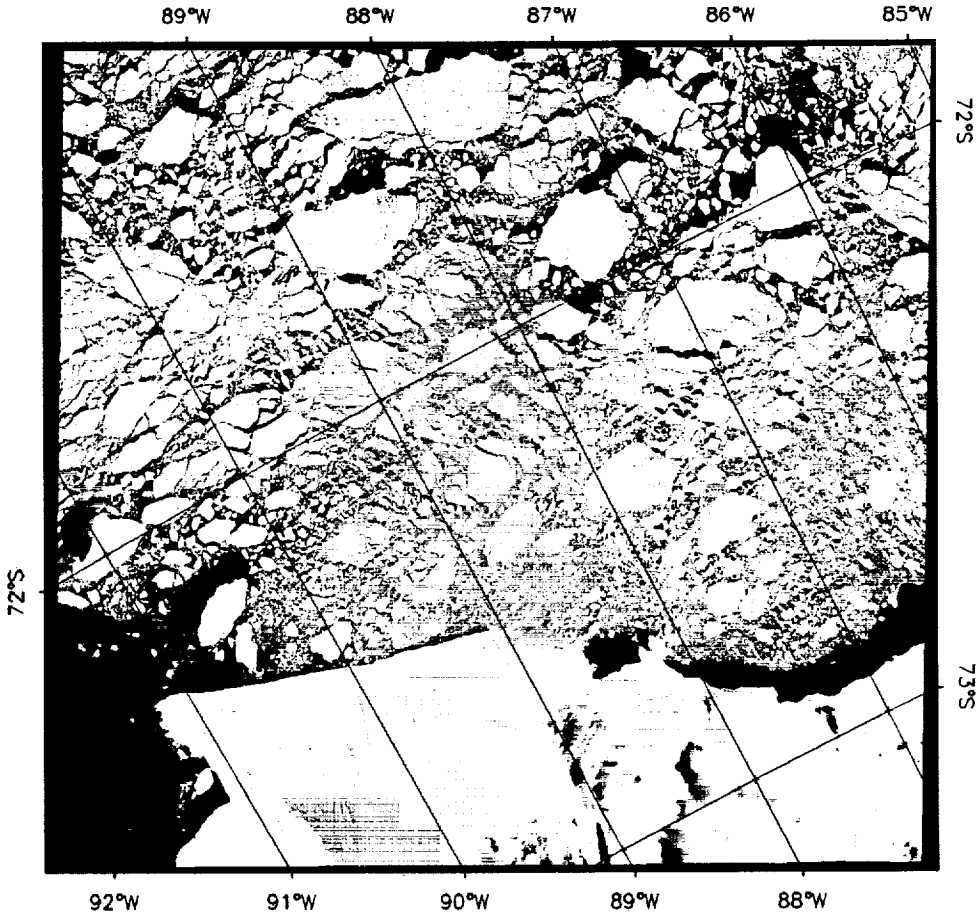

Fig 17: Bellinghausen Sea Dec. 15, 1988

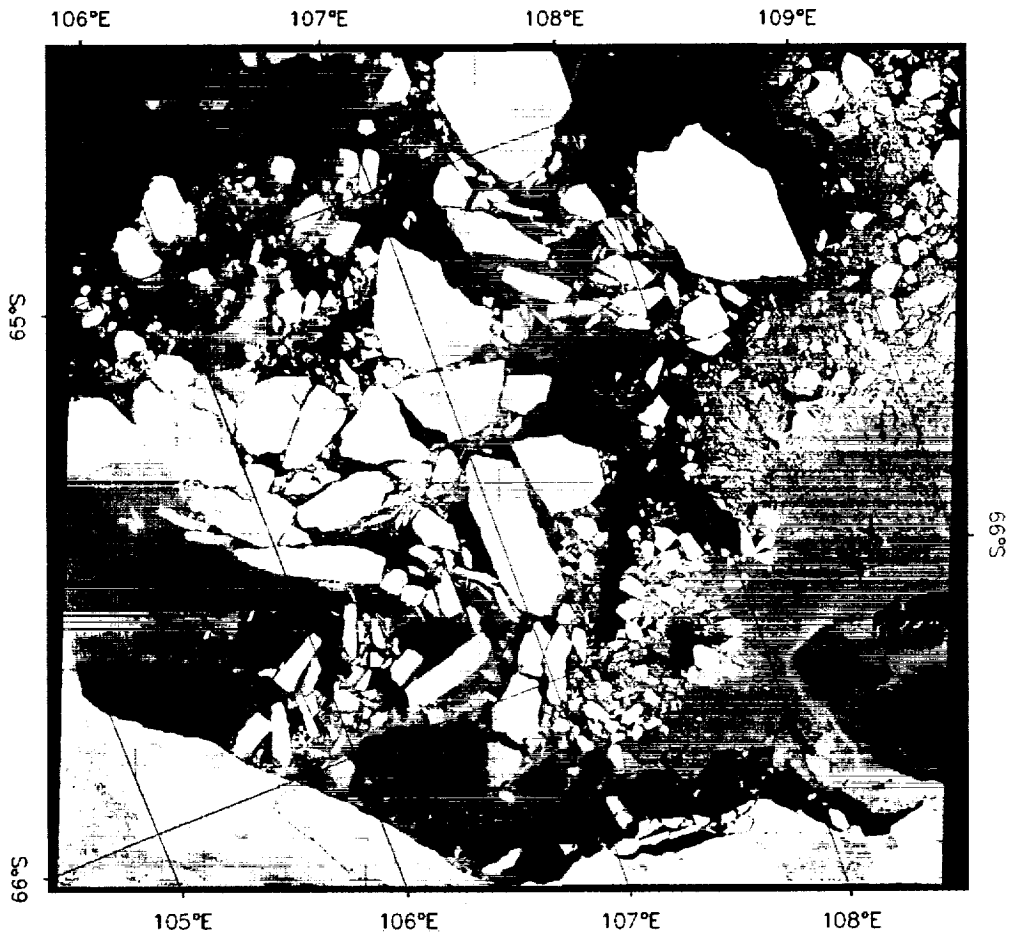

Fig 18: Western Pacific Ocean, Nov 17, 1989

September, 1992

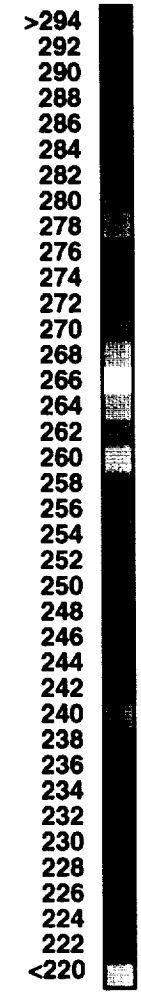

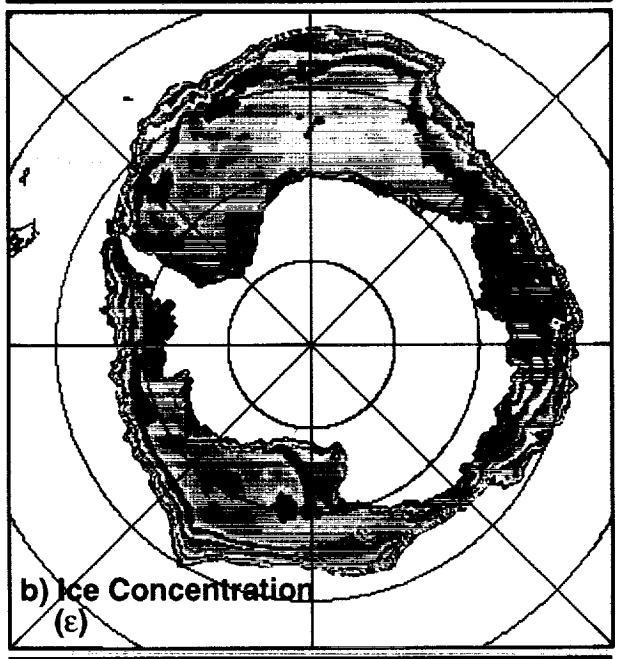

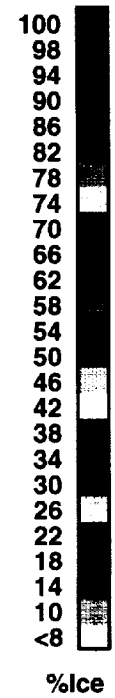

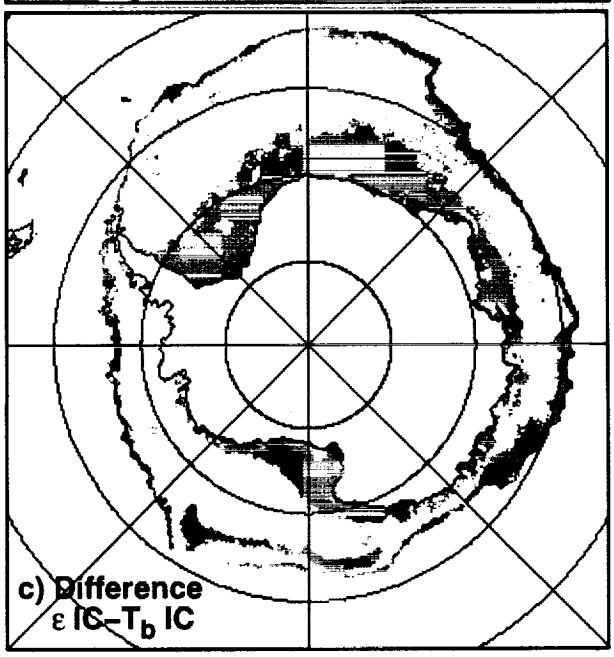

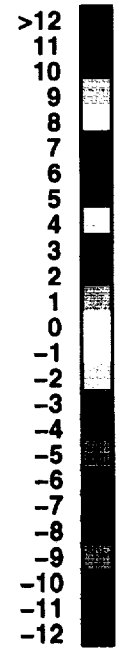

Fig 19

May 21, 1995

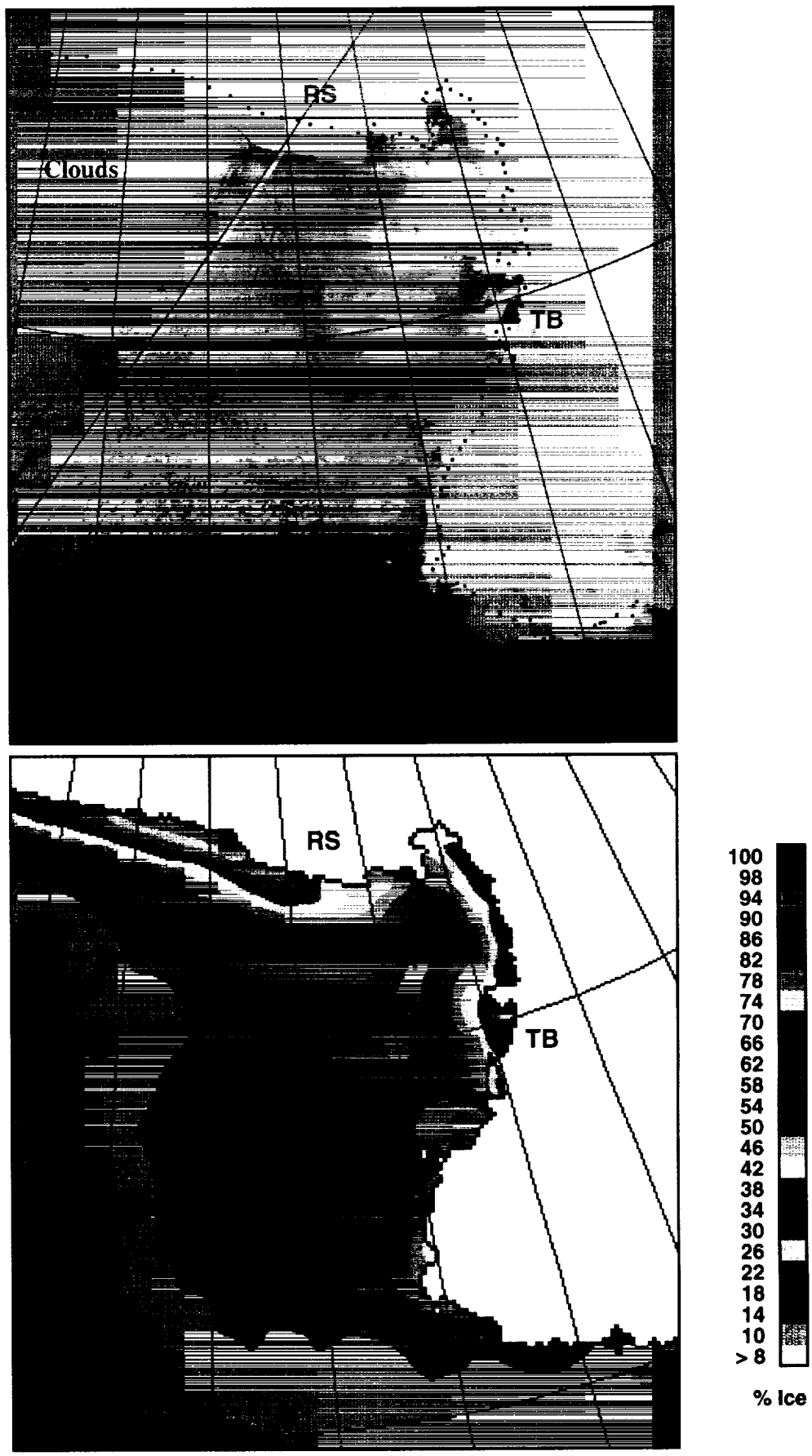

Fig20

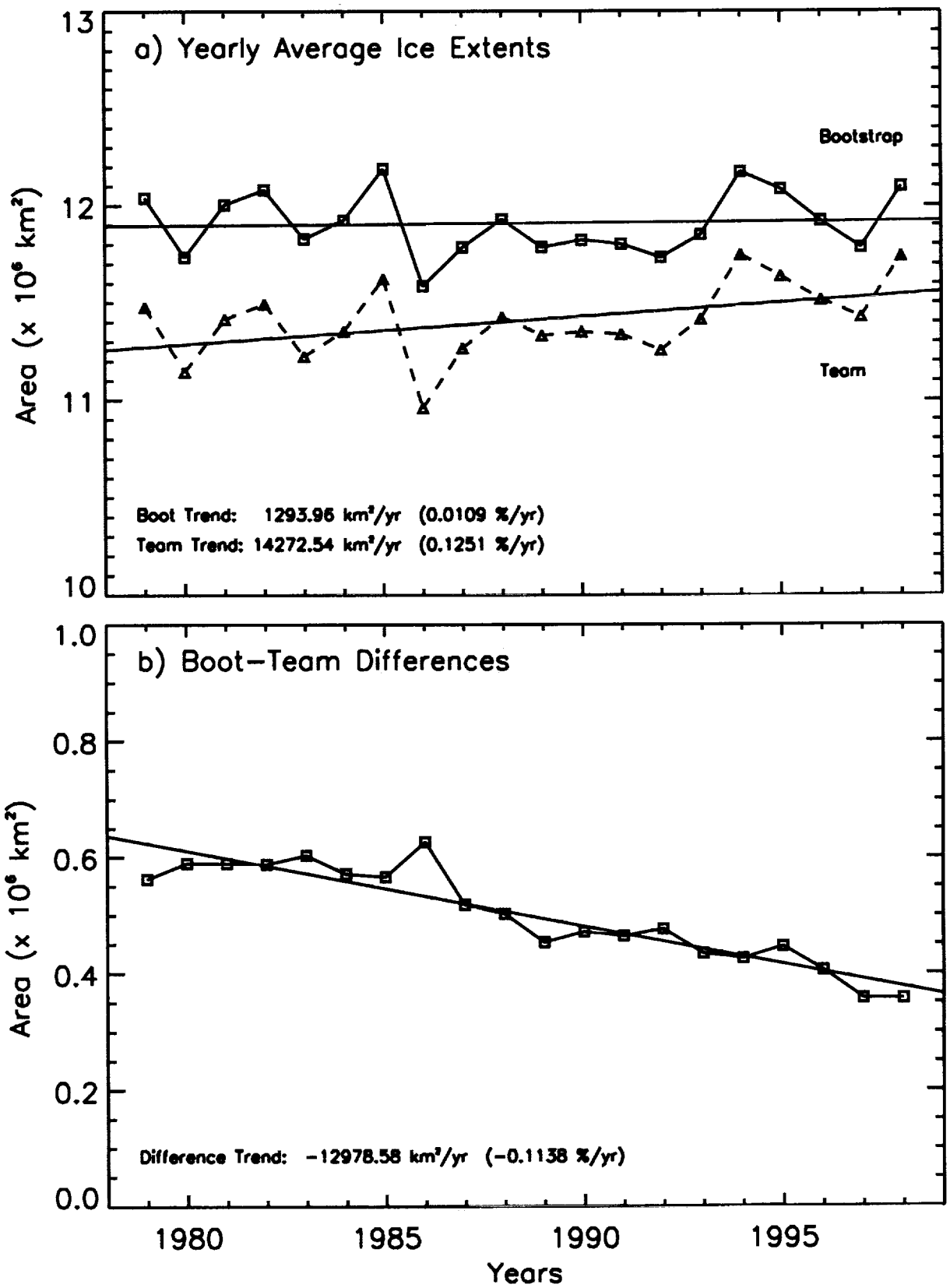
a) Yearly Average Ice Extents
Bootstrap
Team
Boot Trend: 1293.96 km²/yr (0.0109 %/yr)
Team Trend: 14272.54 km²/yr (0.1251 %/yr)
Area (x 10⁶ km²)
13
12
11
10
b) Boot−Team Differences
Difference Trend: −12978.58 km²/yr (−0.1138 %/yr)
Area (x 10⁶ km²)
1.0
0.8
0.6
0.4
0.2
0.0
1980
1985
1990
1995
Years

Fig. 22

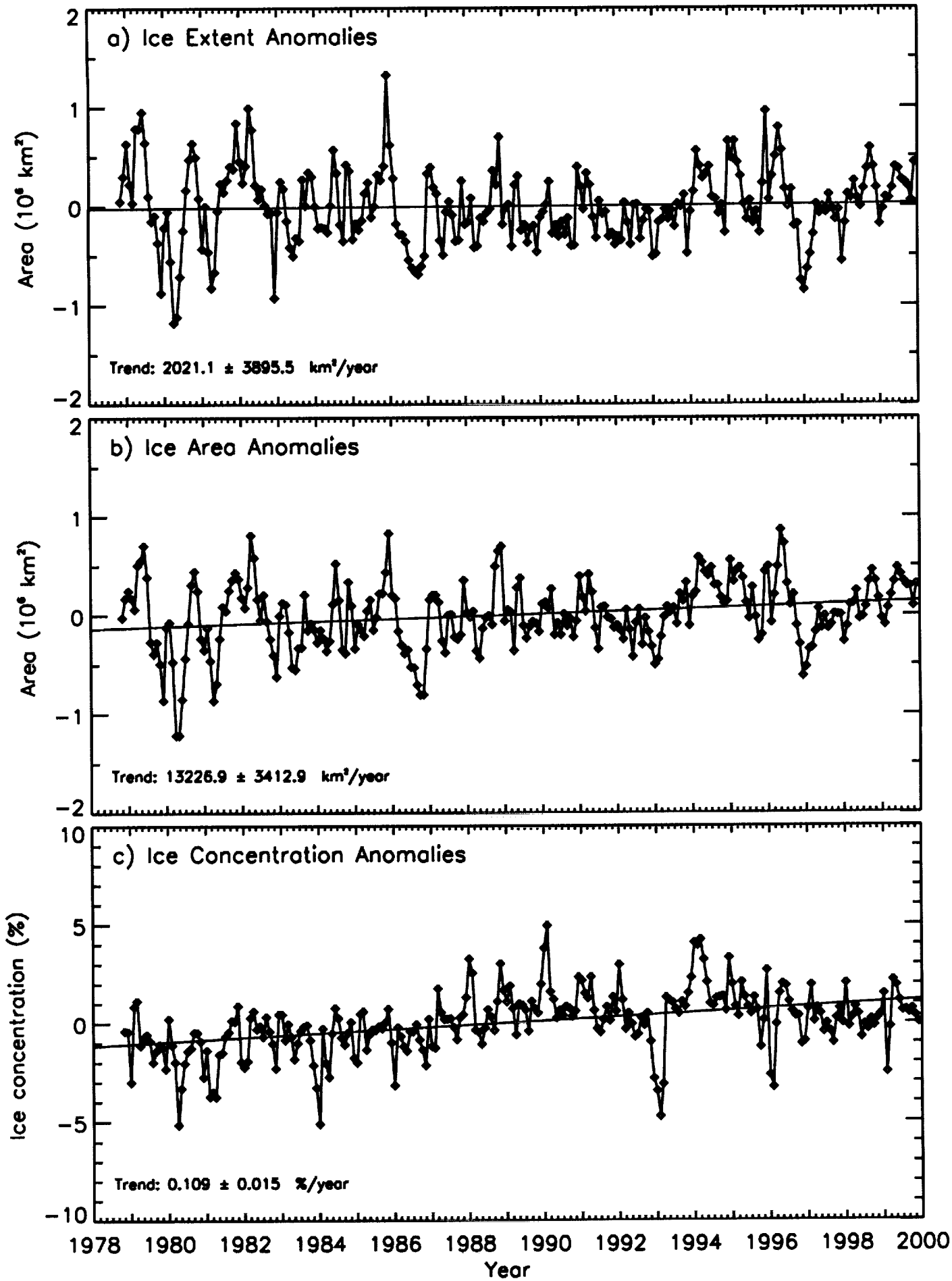
a) Ice Extent Anomalies
Area (10^6 km^2)
Trend: 2021.1 ± 3895.5 km^2/year
b) Ice Area Anomalies
Area (10^6 km^2)
Trend: 13226.9 ± 3412.9 km^2/year
c) Ice Concentration Anomalies
Ice concentration (%)
Trend: 0.109 ± 0.015 %/year
Year

Fig. 23